

See discussions, stats, and author profiles for this publication at: <https://www.researchgate.net/publication/5665205>

# Lipid membrane templates the ordering and induces the fibrillogenesis of Alzheimer's disease amyloid- $\beta$ peptide

ARTICLE *in* PROTEINS STRUCTURE FUNCTION AND BIOINFORMATICS · JULY 2008

Impact Factor: 2.63 · DOI: 10.1002/prot.21887 · Source: PubMed

CITATIONS

66

READS

56

7 AUTHORS, INCLUDING:



**Eva Chi**

University of New Mexico

48 PUBLICATIONS 1,774 CITATIONS

SEE PROFILE



**Jaroslaw Majewski**

University of California, Davis

196 PUBLICATIONS 3,091 CITATIONS

SEE PROFILE



**Guohui Wu**

Unilever

27 PUBLICATIONS 947 CITATIONS

SEE PROFILE



**Ka Yee C. Lee**

University of Chicago

157 PUBLICATIONS 3,928 CITATIONS

SEE PROFILE

# Lipid membrane templates the ordering and induces the fibrillogenesis of Alzheimer's disease amyloid- $\beta$ peptide

Eva Y. Chi,<sup>1</sup> Canay Ege,<sup>1</sup> Amy Winans,<sup>1</sup> Jaroslaw Majewski,<sup>2</sup> Guohui Wu,<sup>1</sup> Kristian Kjaer,<sup>3,4</sup> and Ka Yee C. Lee<sup>1\*</sup>

<sup>1</sup> Department of Chemistry, Institute for Biophysical Dynamics, and The James Franck Institute, The University of Chicago, Chicago, IL 60637

<sup>2</sup> Manuel Lujan Jr. Neutron Scattering Center, Los Alamos Neutron Science Center, Los Alamos National Laboratory, Los Alamos, NM 87545

<sup>3</sup> Max-Planck Institute of Colloids and Interfaces, Am Mühlenberg, Germany

<sup>4</sup> Niels Bohr Institute, University of Copenhagen, Copenhagen, Denmark

## ABSTRACT

The lipid membrane has been shown to mediate the fibrillogenesis and toxicity of Alzheimer's disease (AD) amyloid- $\beta$  (A $\beta$ ) peptide. Electrostatic interactions between A $\beta$ 40 and the phospholipid headgroup have been found to control the association and insertion of monomeric A $\beta$  into lipid monolayers, where A $\beta$  exhibited enhanced interactions with charged lipids compared with zwitterionic lipids. To elucidate the molecular-scale structural details of A $\beta$ -membrane association, we have used complementary X-ray and neutron scattering techniques (grazing-incidence X-ray diffraction, X-ray reflectivity, and neutron reflectivity) in this study to investigate *in situ* the association of A $\beta$  with lipid monolayers composed of either the anionic lipid 1,2-dipalmitoyl-*sn*-glycero-3-[phospho-*rac*-(1-glycerol)] (DPPG), the zwitterionic lipid 1,2-dipalmitoyl-*sn*-glycero-3-phosphocholine (DPPC), or the cationic lipid 1,2-dipalmitoyl 3-trimethylammonium propane (DPTAP) at the air-buffer interface. We found that the anionic lipid DPPG uniquely induced crystal-line ordering of A $\beta$  at the membrane surface that closely

mimicked the  $\beta$ -sheet structure in fibrils, revealing an intriguing templated ordering effect of DPPG on A $\beta$ . Furthermore, incubating A $\beta$  with lipid vesicles containing the anionic lipid 1-palmitoyl-2-oleoyl-*sn*-glycero-3-[phospho-*rac*-(1-glycerol)] (POPG) induced the formation of amyloid fibrils, confirming that the templated ordering of A $\beta$  at the membrane surface seeded fibril formation. This study provides a detailed molecular-scale characterization of the early structural fluctuation and assembly events that may trigger the misfolding and aggregation of A $\beta$  *in vivo*. Our results implicate that the adsorption of A $\beta$  to anionic lipids, which could become exposed to the outer membrane leaflet by cell injury, may serve as an *in vivo* mechanism of templated-aggregation and drive the pathogenesis of AD.

Proteins 2008; 72:1–24.  
© 2008 Wiley-Liss, Inc.

**Key words:** protein aggregation; fibril formation; protein-lipid interactions; protein conformation; lipid vesicles; lipid monolayer; Alzheimer's disease; grazing-incidence X-ray diffraction; X-ray reflectivity.

**Abbreviations:** A $\beta$ , amyloid- $\beta$  peptide; AD, Alzheimer's disease; APP, amyloid precursor protein; CMC, critical micelle concentration; d62-DPPG, tail-deuterated DPPG; DLS, dynamic light scattering; DMSO, dimethyl sulfoxide; DMTAP, 1,2-dimyristoyl-3-trimethylammonium-propane; DPPC, 1,2-dipalmitoyl-*sn*-glycero-3-phosphocholine; DPPG, 1,2-dipalmitoyl-*sn*-glycero-3-[phospho-*rac*-(1-glycerol)]; DPTAP, 1,2-dipalmitoyl 3-trimethylammonium propane; FM, fluorescence microscopy; FWHM, full width at half maximum; GIXD, grazing-incident X-ray diffraction; MALDI, matrix assisted laser desorption/ionization mass spectrometry; NR, neutron reflectivity; PA, palmitic acid; PBS, phosphate buffered saline; POPC, 1-palmitoyl-2-oleoyl-*sn*-glycero-3-phosphocholine; POPG, 1-palmitoyl-2-oleoyl-*sn*-glycero-3-[phospho-*rac*-(1-glycerol)]; RP-HPLC, reverse phase-HPLC; SE-HPLC, size-exclusion high performance liquid chromatography; SLD, scattering length density; TEM, transmission electron microscopy; ThT, Thioflavin-T; XR, X-ray specular reflectivity.

Grant sponsor: Alzheimer's Association; Grant number: IIRG-9901175; Grant sponsor: American Health Assistance Foundation; Grant number: A1999057; Grant sponsor: US Department of Energy; Grant number: W-7405-ENG-36; Grant sponsor: National Institute of Health; Grant number: AG025649; Grant sponsor: National Science Foundation Materials Research and Engineering Centers Programs; Grant number: DMR-0213745; Grant sponsors: Packard Foundation, Beckman Scholars Program; GW acknowledges the support of Burroughs Wellcome Fund Interfaces No. 1001774.

EYC and CE contributed equally to this work.

\*Correspondence to: Ka Yee C. Lee, Department of Chemistry, The University of Chicago, 929 E. 57th Street, Chicago, IL 60637. E-mail: kayeelee@uchicago.edu

Received 27 July 2007; Revised 26 September 2007; Accepted 23 October 2007

Published online 10 January 2008 in Wiley InterScience (www.interscience.wiley.com). DOI: 10.1002/prot.21887

## INTRODUCTION

The misfolding, aggregation, and accumulation of the amyloid- $\beta$  peptide ( $A\beta$ ) into insoluble deposits have been implicated as the primary cause of neuronal death in Alzheimer's disease (AD).<sup>1</sup> In addition to AD, more than 20 degenerative disorders affecting either the central nervous system (e.g., Parkinson's disease, Huntington's disease, and transmissible prion diseases) or a variety of peripheral tissues (e.g., diabetes, liver cirrhosis, and degenerative eye diseases) share the same general pathology, each arising from the aggregation of an associated protein.<sup>1–3</sup> Although proteins implicated in these diseases share no structural or sequence homology, one defining feature is that they all aggregate into highly ordered insoluble fibrils containing extensive  $\beta$ -sheet structures.<sup>1,4,5</sup> The large body of research performed during the past 10 years has significantly increased our understanding of the pathways involved in  $A\beta$  aggregation and the mechanism of cellular toxicity.<sup>1,6–8</sup> However, the molecular basis of the early events during the aggregation process and the nature of the structural fluctuations that triggers the misfolding and association of  $A\beta$  remain poorly understood.

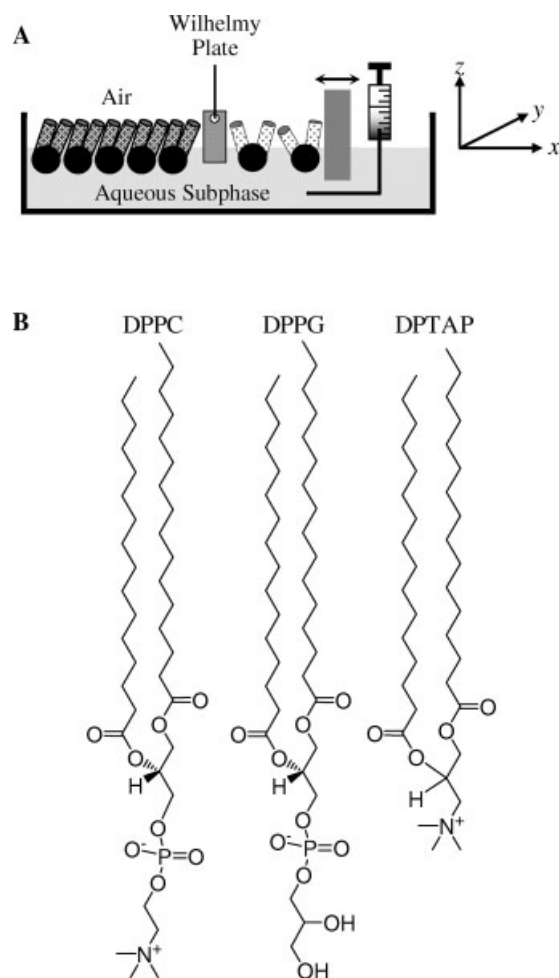
$A\beta$  is a 40- to 43-amino acid residue peptide derived from the proteolytic processing of the transmembrane amyloid precursor protein (APP) during regular cell metabolism.<sup>9</sup> The peptide is amphiphilic, with a hydrophilic N-terminal region and a hydrophobic C-terminal region that belongs to the transmembrane domain of APP. The assembly of native  $A\beta$  into fibrillar deposits is accompanied by substantial changes to the peptide conformation. Under conditions that mimic the cell membrane, where the C-terminus of  $A\beta$  resides before it is cleaved from APP,  $A\beta$  exhibits a significant amount of  $\alpha$ -helical structure.<sup>10,11</sup> When assembled into fibrils,  $A\beta$  adopts the characteristic  $\beta$ -sheet structures found in amyloid fibrils.<sup>12,13</sup> In physiological buffers at low  $A\beta$  concentrations, the peptide is largely a random, flexible chain,<sup>14</sup> with some local structural motifs.<sup>15,16</sup> Thus, regardless of the conformation the native  $A\beta$  adopts, the emergence of cytotoxic  $A\beta$  aggregates necessitates the formation of inter- and intra-molecular  $\beta$ -sheets.

*In vitro*,  $A\beta$  fibrillogenesis has been found to proceed through a nucleation-dependent polymerization mechanism characterized by an initial lag phase.<sup>17,18</sup> Fibril formation occurs readily at concentrations above a "critical micelle concentration" (CMC) that has been found to range from 17.5 to 100  $\mu$ M,<sup>18–20</sup> after which fibrils nucleate within these micelles.<sup>18</sup> The lag phase, to a significant degree, reflects the energy barrier that must be overcome in order for the otherwise unfolded  $A\beta$  to adopt a  $\beta$ -sheet rich conformation and oligomerize into ordered intermediates or protofibrils.<sup>17,21–24</sup> *In vivo*, the concentration of free  $A\beta$  in the cerebral spinal fluid is exceedingly low, in the subnanomolar concentration range.<sup>25</sup> Since the  $A\beta$  concentration required for homogeneous nucleation differs from the  $A\beta$  concentration found *in vivo* by several orders

of magnitude, the onset of  $A\beta$  fibrillogenesis *in vivo* likely proceeds by an alternative mechanism.

There is increasing evidence that the cell membrane plays a central role in mediating  $A\beta$  fibrillogenesis.<sup>26–29</sup> It has been shown that membrane lipids extracted from human brain cells can accelerate  $A\beta$  fibril formation and that the composition of lipid membranes controls  $A\beta$ -lipid interactions and fibrillogenesis.<sup>29–31</sup> One characteristic that has been well documented is the effect of lipid headgroup charge on  $A\beta$  fibril formation. Compared with zwitterionic lipids, anionic lipids have been shown to enhance  $A\beta$ 's association with and insertion into lipid membranes,<sup>27,32,33</sup> inducing the formation of  $\beta$ -sheets,<sup>26,27,33,34</sup> and promoting the formation of  $A\beta$  fibrils.<sup>35,36</sup> The association of  $A\beta$  to negatively charged lipids is dominated by electrostatic attraction<sup>32,33,37</sup> and the phosphate group on the lipid headgroup has been found to be essential for  $A\beta$  binding.<sup>35</sup> In addition to mediating  $A\beta$  fibril formation, the interaction of the peptide with cell membranes may also serve as a pathway by which  $A\beta$  exerts toxicity. One proposed mechanism for  $A\beta$  neurotoxicity is membrane disruption and depolarization mediated by either ion-channel formation or an increase in overall membrane conductance, resulting in the alteration of ion homeostasis and dysregulation of neuronal signal transduction, leading to cell death.<sup>38–43</sup>

To fully understand the effect of lipid headgroup charge on  $A\beta$ -membrane interactions, we used lipid monolayers at the air-water interface [Fig. 1(A)], which model the outer leaflet of the cell membrane, to probe  $A\beta$  interaction with lipid membrane and to characterize  $A\beta$ -induced alterations in membrane morphology and lipid packing. In an earlier study,<sup>32</sup> we reported that monomeric  $A\beta$ 40 spontaneously inserted into lipid monolayers composed of either the anionic lipid 1,2-dipalmitoyl-*sn*-glycero-3-[phospho-*rac*-(1-glycerol)] (DPPG) or the cationic lipid 1,2-dipalmitoyl 3-trimethylammonium propane (DPTAP) at bilayer-equivalent lipid densities (e.g., monolayer surface pressure of 30 mN/m<sup>32,44</sup>) whereas the insertion of  $A\beta$  into the zwitterionic lipid 1,2-dipalmitoyl-*sn*-glycero-3-phosphocholine (DPPC) occurred at surface pressures well below that found in a lipid bilayer (e.g., 23 mN/m). Structures of these different lipids are shown in Figure 1(B). Phospholipids in the cell membrane usually contain one tail that is unsaturated.<sup>45</sup> The saturated lipids were chosen for our monolayer studies because they undergo phase transition to form condensed domains when compressed to 30 mN/m, thus allowing us to use membrane morphology to gauge the extent of lipid-peptide interaction upon the introduction of  $A\beta$  in the subphase. Using fluorescence microscopy (FM), we found that the association and insertion of  $A\beta$  into lipid monolayers can induce a near complete disruption of monolayer morphology and that in some cases, inserted  $A\beta$  colocalized with the disordered region of the lipid monolayer.<sup>32</sup> These results confirmed that the elec-

**Figure 1**

(A) Schematic of a Langmuir trough containing a lipid monolayer. The movable barrier controls the lipid density of the film and the Wilhelmy plate measures the surface pressure ( $\pi$ ), where  $\pi = \gamma_0 - \gamma$  and  $\gamma_0$  is the air-water surface tension and  $\gamma$  is the lipid film surface tension. A syringe with an L-shaped needle was used to inject protein into the subphase. (B) Structures of the lipids used. The lipids have identical saturated 16-carbon acyl chains but differ in their headgroup architecture and charge.

trostatic interaction between A $\beta$  and the lipid headgroup strongly mediates A $\beta$ -membrane interactions and implicated that charged lipids may play a role in A $\beta$  fibrillogenesis and toxicity.

Although pressure-area measurements and FM imaging of A $\beta$  association with lipid monolayers gave us valuable information on A $\beta$ -lipid interactions and micron-scale monolayer morphology,<sup>32</sup> they offered limited insights regarding the molecular-scale structural details of the protein-lipid films. Our initial attempt to obtain these structural details has led us to apply X-ray scattering techniques to examine A $\beta$ -phospholipid monolayers and our data revealed an intriguing templating effect of the anionic lipid DPPG on A $\beta$  in water.<sup>34</sup> In this current study, we have expanded upon this earlier work by incor-

porating several complementary surface sensitive X-ray and neutron scattering techniques, including grazing-incidence X-ray diffraction (GIXD), X-ray specular reflectivity (XR), and neutron specular reflectivity (NR), to investigate *in situ* A $\beta$ -lipid films at the air-subphase interface on either water or the more physiologically relevant solution condition of phosphate buffered saline (PBS, pH 7.4, 10 mM sodium phosphate, 3 mM potassium chloride, and 138 mM sodium chloride). All experiments were carried out at 30°C and an A $\beta$  concentration of 250 nM that is well below its documented CMC to better mimic *in vivo* A $\beta$  concentration. GIXD measurements provide structural information on the in-plane (i.e., in the plane of the monolayer) crystalline (hence diffracting) portion of the film, while XR measurements yield information about the out-of-plane (z-direction) monolayer structure, laterally averaged over both crystalline and amorphous portions.<sup>46,47</sup> Additionally, NR experiments were carried out to provide complementary information on out-of-plane structures.<sup>48</sup> Combining these scattering techniques allowed for the first complete, angstrom-scale, characterization of A $\beta$ 's association with different charged lipids.

Our results confirmed that the anionic lipid DPPG uniquely templated the folding and ordering of A $\beta$  into  $\beta$ -sheet crystalline structures at the lipid surface. To evaluate whether these templated structures can trigger the aggregation of A $\beta$  with a more physiological membrane system, the peptide was incubated with lipid vesicles comprised of mono-unsaturated and more fluid lipids. Vesicles were made up of either the zwitterionic lipid 1-palmitoyl-2-oleoyl-*sn*-glycero-3-phosphocholine (POPC), or POPC containing either 30 mol% of the anionic lipid 1-palmitoyl-2-oleoyl-*sn*-glycero-3-[phospho-*rac*-(1-glycerol)] (POPG), or 30 mol% of the cationic lipid 1,2-dimyristoyl-3-trimethylammonium-propane (DMTAP). Charged lipids were used in combination with the neutral lipid POPC because charged lipids alone do not form stable vesicles. Size distributions of the vesicles, the adsorption of A $\beta$  to vesicles, and A $\beta$  fibril formation and morphology were monitored with incubation time using a number of analytical techniques.

## METHODS

### Materials

The lipids DPPC, DPPG, DPTAP, palmitic acid (PA), tail-deuterated DPPG (d62-DPPG), POPC, POPG, and DMTAP were purchased from Avanti Polar Lipids (Alabaster, AL). PA and Thioflavin-T (ThT) were purchased from Sigma-Aldrich (St. Louis, MO). PBS was purchased from Invitrogen (Carlsbad, CA). All water used was filtered through a Milli-Q Ultrapure water purification system from Millipore (Bedford, MA).

A $\beta$ 40 peptide (amino acid sequence of DAEFRHDS-GYEVHHQKLFFAEDVGSNKGAIIGLMVGGVV) used



for X-ray and neutron scattering experiments was purchased from AnaSpec (San Jose, CA) and used without further purification. Purity was reported to be 95%. The molecular weight of the peptide was confirmed by matrix assisted laser desorption/ionization (MALDI) mass spectrometry. A $\beta$  was stored at  $-20^{\circ}\text{C}$  in lyophilized form until use. A $\beta$ 40 used for the incubation experiments was synthesized using 9-fluorenylmethoxycarbonyl chemistry on an Applied Biosystems 433A Peptide Synthesizer (Foster City, CA). Peptides were purified by reverse phase-HPLC (RP-HPLC) on a preparative Zorbax C18 column at  $60^{\circ}\text{C}$ . Peptide sequence was confirmed by a mass spectrometry-based protein identification method where purified A $\beta$  was first digested with trypsin and followed by RP-HPLC and mass spectrometry/mass spectrometry analysis. Peptide mass was confirmed by MALDI mass spectrometry and peptide purity was determined by analytical RP-HPLC to be 90% or higher. Purified A $\beta$  was lyophilized and stored at  $-20^{\circ}\text{C}$  until use.

To ensure the complete dissociation of A $\beta$  into monomers, A $\beta$  was first dissolved in dimethyl sulfoxide (DMSO) to yield a stock solution of 5 mg/mL.<sup>24,32,49</sup> Importantly for our study, DMSO did not exhibit any surface activity. The stock A $\beta$  solution was subsequently diluted with an appropriate buffer for X-ray scattering experiments or a vesicle solution for incubation experiments.

### X-ray scattering experiments

All X-ray scattering experiments were carried out on the BW1 beam line at the HASYLAB synchrotron source (DESY Deutsches Elektronen-Synchrotron, Hamburg, Germany) with a dedicated liquid surface diffractometer.<sup>47,50–52</sup> A temperature-controlled Langmuir trough was mounted on the diffractometer. The trough was equipped with a Wilhelmy plate balance for measuring the surface pressure ( $\pi$ ) and a Teflon barrier for changing the surface area. All experiments were carried out at  $30^{\circ}\text{C}$ . The X-ray beam that illuminates the sample had a wavelength ( $\lambda$ ) of  $\sim 1.3 \text{ \AA}$  and a power of  $\sim 0.3 \text{ mW}$ .

After calibrating the Wilhelmy plate pressure sensor at  $30^{\circ}\text{C}$ , 240 mL of aqueous subphase was decanted into the trough. To damp mechanically excited long wavelength waves on the liquid surface, a glass block was placed in the trough such that the water thickness above the glass block was less than 1 mm. To minimize the adsorption of A $\beta$  to glass surface, the glass block was coated with polyethylene glycol. In between X-ray experiments, the glass block was cleaned by sonication in a dilute soap solution followed by a thorough rinse with Milli-Q water.

DPPC and DPTAP dissolved in chloroform (HPLC grade, Fisher Scientific) and DPPG dissolved in chloroform containing 10% methanol (Fisher Scientific) were spread at the air–water interface. The system was allowed to equilibrate for 15 min to ensure the complete evaporation of the organic solvent, after which the lipid mono-

layer was compressed to 23 or 30 mN/m. Once the desired surface pressure was reached, pressure was kept constant via a feedback loop. An aliquot of A $\beta$  in a matching solution was then injected into the subphase of the trough using a L-shaped syringe underneath the barrier to avoid disturbing the lipid film [Fig. 1(A)]. A $\beta$  concentration in the subphase was 250 nM for all experiments. After injecting A $\beta$ , trough area was recorded, from which changes in the effective area per lipid molecule ( $\Delta A/A = (A_{\text{final}} - A_{\text{initial}})/A_{\text{initial}}$ ) compared with those before A $\beta$  injection was calculated. To prepare lipid monolayers for X-ray measurements, the trough canister was purged for 30–40 min with helium to reduce background scattering from the gas phase and prevent oxidative beam damage during X-ray scans. Oxygen level was kept lower than 1%. To further reduce beam damage, the trough was translated by 0.025 mm in the horizontal direction after every step during GIXD scans and by 2 mm during XR scans.

To maximize the surface sensitivity of GIXD measurements, the incidence angle of the X-ray beam ( $\alpha_i$ ) was  $0.85\alpha_c$ , where  $\alpha_c \sim 0.13^{\circ}$  is the critical angle for total external reflection.<sup>53</sup> The footprint of the incoming X-ray beam on the surface was  $\sim 2 \times 50 \text{ mm}^2$ . Diffracted intensities were collected using a one-dimensional position-sensitive detector (PSD, OEM-100-M, Braun, Garching, Germany) as a function of the vertical scattering angle and has a measuring window of  $0 < q_z < 1.3 \text{ \AA}^{-1}$ . A Soller collimator was mounted in front of the PSD, which gave a horizontal resolution of the detector of  $\Delta q_{xy} = 0.0084 \text{ \AA}^{-1}$ . Scattering intensity was measured by scanning over a range of the horizontal scattering vector component  $q_{xy}$ , and simultaneously recording the entire range of  $q_z$  of the PSD.

For XR measurements, an additional slit is used to exclude diffusely scattered background around the reflected beam. This slit, together with a scintillation detector having a thin vertical measuring window (with a  $q_z$  resolution of  $\sim 0.1 q_c$ , where  $q_c$  is  $0.022 \text{ \AA}^{-1}$ ), is mounted on an elevator situated on a diffractometer arm, which is pivoted around a vertical axis through the sample center. A Soller collimator was not used for XR measurements.

### Neutron reflectivity measurements

NR experiments were carried out on the horizontal reflectometer beamline (NG7) at the National Institute of Standards and Technology in the Center for Neutron Research (Gaithersburg, MD). Using a  $4.75 \text{ \AA}$  wavelength neutron beam from a reactor source, the reflectivity of the lipid film as a function of  $q_z$  values from 0.01 to  $0.20 \text{ \AA}^{-1}$  was collected. Scanning time for this  $q_z$  range was 3–4 h. The reflected neutrons were counted using an Ordela position-sensitive  $^3\text{He}$  detector (Ordela, Oak Ridge, TN).

### A $\beta$ incubation with large unilamellar vesicles

To investigate the effect of the different charged lipids on A $\beta$  fibril formation, the peptide was incubated with vesicles composed of POPC, POPC containing 30 mol% POPG, or POPC containing 30 mol% DMTAP in either water or PBS at 25°C. To prepare lipid vesicles, desired amounts of lipids were first dissolved in chloroform, dried under a stream of nitrogen, and further dried under vacuum overnight. The lipids were then hydrated with water, put through five freeze-thaw cycles, and extruded 19 times using an extruder with 100-nm pore size polycarbonate membranes (Avanti Polar Lipids, Alabaster, AL) to yield large unilamellar vesicles.

Stock A $\beta$ 40 dissolved in DMSO was added to each vesicle solution to yield incubation mixtures containing 100  $\mu$ M A $\beta$  with 1:20 peptide to lipid mole ratio. Samples were then incubated at 25°C without agitation. Control samples of A $\beta$  alone and vesicles alone were also prepared and incubated. At each time point, an aliquot of each sample was taken and the size distribution of vesicles, the amount of soluble A $\beta$  remaining, and the presence of fibrils were determined using a number of analytical methods.

To evaluate changes in vesicle size during incubation with A $\beta$ , size distribution of samples and controls were measured by dynamic light scattering (PD2000DLS Detector, Precision Detectors, Franklin, MA). To assess the extent of soluble A $\beta$  depletion from solution because of adsorption onto vesicles and formation of fibrils, the amount of soluble A $\beta$  remaining in each sample was analyzed by size exclusion-HPLC (SE-HPLC). Samples were first centrifuged at 15,000 rpm for 10 min to remove insoluble materials. Supernatant was then injected onto a BioSep-SEC-S2000 column (Phenomenex, Torrance, CA) and chromatograms were collected as UV absorbance at 215 and 280 nm. Peak area in the chromatogram was used to quantify the amounts of soluble A $\beta$  in the samples. The amount of protein present was calculated by dividing the measured peak area by the peak area for an unincubated control sample.

To monitor the formation of A $\beta$  fibrils, ThT fluorescence of incubated samples were measured on a Fluoromax-3 spectrofluorometer (Horiba Jobin Yvon, Edison, NJ). At each time point, 20  $\mu$ L of a sample incubated in either water or PBS was mixed with 2 mL of 10  $\mu$ M ThT in either pH 5.5 10 mM sodium acetate with 140 mM sodium chloride or PBS. Fluorescence emission intensity of the sample were immediately recorded for 10–30 min ( $\lambda_{\text{ex}} = 446 \pm 3$  nm,  $\lambda_{\text{em}} = 490 \pm 10$  nm).<sup>24,49</sup> ThT fluorescence of control samples, A $\beta$  alone and vesicles alone, were also collected to enable proper background subtraction.

To image the morphology of A $\beta$  aggregates formed, transmission electron microscopy (TEM) was used. Samples were diluted five times and applied to a glow-discharged carbon-coated support film, washed with water,

stained with 1% uranyl acetate for 30 s, and then dried. Micrographs were recorded using a FEI Tecnai F30 scanning transmission electron microscope (FEI Company, Hillsboro, OR).

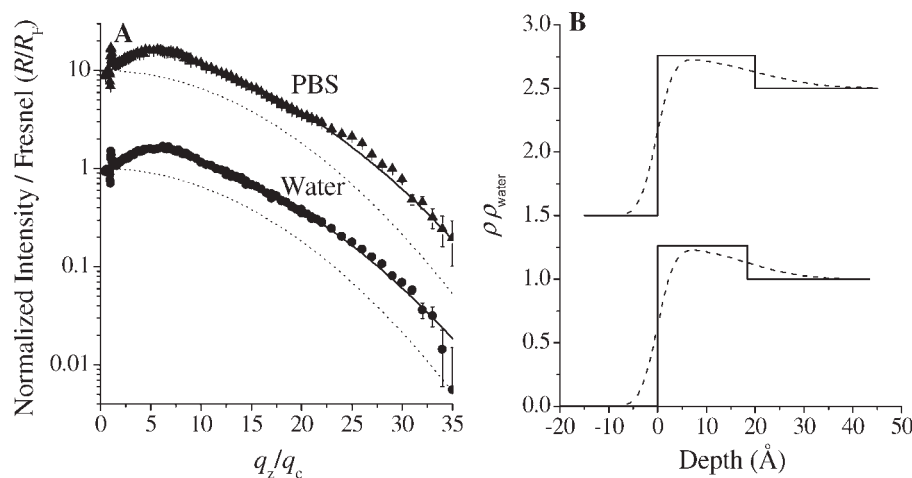
## RESULTS

### Analysis and interpretation of X-ray and neutron scattering data

From XR data, detailed information on the electron density distribution [ $\rho(z)$ ], in the  $z$ -direction of the lipid membrane laterally averaged over the entire film ( $xy$  plane) [Fig. 1(A)], can be obtained from modeling the ratio,  $R/R_F$ , between the measured reflectivity ( $R$ ) and Fresnel's reflectivity ( $R_F$ ) calculated for a perfectly sharp interface between air and a pure subphase.<sup>46,47,54</sup> The simplest, and physically reasonable, model to fit  $R/R_F$  is a stack of homogeneous slabs, where each slab represents a chemically distinct moiety of a molecule (e.g., a lipid headgroup) with constant electron density  $\rho$  and a characteristic thickness ( $L$ ).<sup>50–52</sup> To account for the vertical roughness, or diffuseness ( $\sigma$ ), of the interface between the different slabs,  $\rho(z)$  was “smeared” in the  $z$ -direction by convolution with a Gaussian function of the root-mean-square with  $\sigma$ . A  $\sigma$  value of ca. 3 Å for most lipid monolayers mainly stems from thermally excited capillary waves on the liquid surface.<sup>55,56</sup> Fitting the slab model to  $R/R_F$  data yields parameters characterizing the vertical structure of a 2D film— $\rho$  and  $L$  of each molecular layer and  $\sigma$  of the inter-layer interface. Because each slab introduces three parameters, fitting can easily become over-parameterized as the number of slabs is increased to model the physical system. A criterion used in our fitting was to produce the best fit with the fewest parameters possible. In the cases where multiple slabs were needed, e.g., lipid head group, lipid tails, adsorbed protein, and inserted protein, as many parameters as possible were fixed with known values to minimize the problem of over-parameterization.

Analogous to XR, NR yields angstrom-level information along the  $z$ -direction of a thin film. Instead of the scattering of X-ray by electrons, neutrons are scattered by atomic nuclei.<sup>48</sup> Modeling of NR data gives the scattering length density (SLD) distribution of atomic nuclei in the  $z$ -direction. NR data were also analyzed using the slab model and three parameters were extrapolated from each slab: SLD,  $L$ , and  $\sigma$ .

In GIXD diffracted intensity from an incident X-ray beam that is totally externally reflected is collected over a range of the horizontal scattering vector component  $\{q_{xy} \approx (2\pi/\lambda) [1 + \cos^2(\alpha_f) - 2 \cos(\alpha_f) \cos(2\theta_{xy})]^{1/2}\}$  and of the vertical scattering component  $[q_z \approx (2\pi/\lambda) \sin(\alpha_f)]$ , where  $2\theta_{xy}$  is the horizontal scattering angle and  $\alpha_f$  is the vertical exit angle. Integrating the scattering intensity  $I(q_{xy}, q_z)$  over  $q_z$  yields Bragg peaks and integrating over

**Figure 2**

XR data and fit of A $\beta$  in water (●) and PBS (▲) adsorbed to the air-subphase interface at 30°C (A). For comparison, the reflectivity profile of a bare air-water interface with a 3 Å roughness (Fresnel curve) (dotted line) was also plotted. The solid lines represent fitted reflectivity curves. Corresponding electron density profiles of A $\beta$  in water (lower plot) and PBS (upper plot) obtained from one-slab model fitting of XR data (B). Both unsmeared (solid line) and smeared (dotted line) electron density profiles were plotted. Depth at 0 Å corresponds to the air-A $\beta$  interface. XR data and electron density profiles have been vertically offset for clarity.

$q_{xy}$  across a Bragg peak gives rise to the corresponding Bragg rod profile  $I(q_z)$ .<sup>46,47,54</sup> The  $q_{xy}$  position of a Bragg peak is used to calculate the repeat distances ( $d$ -spacings,  $d = 2\pi/q_{xy}$ ) for the 2D crystalline structure and the full width at half maximum [FWHM( $q_{xy}$ )] of the Bragg peaks yields the coherence length [ $L_{xy} = 0.89 \cdot 2\pi/\text{FWHM}(q_{xy})$ ] of the 2D crystallites, that is, the average size of diffracting crystals. Bragg rod profile can be used to extract important structural information on the molecular crystalline arrangement in a monolayer, such as the tilt angle and tilt direction of lipid tails around the surface normal.<sup>47</sup> Additionally, FWHM of a Bragg rod [FWHM( $q_z$ )] can be used to estimate the length of the molecule that scatters coherently.<sup>47</sup>

### A $\beta$ adsorbed to the air-water interface

The amphiphilic A $\beta$ 40 readily adsorbed to the air-water interface when injected into the aqueous subphase of a Langmuir trough. At 250 nM, A $\beta$  equilibrated to final surface pressures of 12 and 15 mN/m in water and PBS, respectively.<sup>32</sup> The XR data for surface-adsorbed A $\beta$  are shown in Figure 2(A). A one-slab model, the simplest physically reasonable model, was used to fit both data sets; fitting parameters are summarized in Table I. For comparison, the reflectivity of a bare air-water interface with a  $\sigma$  value of 3 Å was also plotted [Fig. 2(A), dotted line]. Note that  $\rho_{\text{PBS}}$  is comparable, higher by one part in 1000, to  $\rho_{\text{water}}$ . Calculations were therefore all carried out with  $\rho_{\text{water}}$  for both water and PBS subphase conditions. The  $\rho(z)$  profiles, unsmeared (solid lines) and smeared (dashed lines), obtained from the slab

model are shown in Figure 2(B). In the  $\rho(z)$  profiles, the hydrophobic-hydrophilic interface was designated as  $z = 0$ . In this case,  $z = 0$  coincided with the air-A $\beta$  interface [Fig. 2(B)]. According to this  $z$ -scale, negative  $z$  values represent the hydrophobic portion of the film (e.g., air and lipid tails) and positive  $z$  values represent the hydrophilic portion of the film (e.g., A $\beta$  and lipid headgroups). XR data of the adsorbed peptide could be fit with a one-slab model [Fig. 2(B) and Table I]. The thicknesses of the A $\beta$  layers adsorbed to the air-subphase interface from water and PBS were  $18.6 \pm 1.6$  and  $20.2 \pm 2.4$  Å, respectively. The  $\sigma$  values of the A $\beta$ -air interface were close to the 3 Å expected from the thermal excitation of capillary waves (Table I). However,  $\sigma$  values of the A $\beta$ -subphase interface were significantly higher,  $\sim 10$  Å. These increased  $\sigma$  values indicated that there was either a concentration gradient of the peptide at the interface or that a portion of the peptide, likely the unstructured N-terminus,<sup>13,57</sup> extended into the subphase.

A $\beta$  adsorbed to the air-water interface exhibited lateral crystalline ordering, giving rise to two Bragg peaks in the GIXD data [Fig. 3(A)]. Each of the background subtracted peaks could be fit with a single Gaussian, indicative of one characteristic  $d$ -spacing. The peaks were located at  $q_{xy} = 0.17$  and  $1.32 \text{ \AA}^{-1}$  (see Fig. 3), corresponding to  $d$ -spacings of 36.2 and 4.76 Å, respectively (Table II). Fibril formation was not expected at the low A $\beta$  concentration of 250 nM used in our experiments; surprisingly the  $d$ -spacing of 4.76 Å closely matched the  $\beta$ -sheet spacing between A $\beta$  monomers in an amyloid fiber.<sup>5,13,58</sup> Evidence of air-water interface induced

**Table I**  
Fitting Parameters for XR Data of A $\beta$  and Single Component Lipid Films at the Air-Subphase Interface at 30°C

Sample	Water subphase					PBS subphase					
	$\pi$ (mN/m)	Headgroup region		Tail region		$\pi$ (mN/m)	Headgroup region		Tail region		
		Thickness $L_h$ (Å)	$\rho_h/\rho_{\text{water}}$	Thickness $L_t$ (Å)	$\rho_t/\rho_{\text{water}}$		Thickness $L_h$ (Å)	$\rho_h/\rho_{\text{water}}$	Thickness $L_t$ (Å)	$\rho_t/\rho_{\text{water}}$	
A $\beta$	12	18.6 $\pm$ 1.6	1.26 $\pm$ 0.01			15	20.2 $\pm$ 2.4	1.26 $\pm$ 0.03			10.60 $\pm$ 2.36 2.76 $\pm$ 0.07 <sup>c</sup>
DPPC	23	6.6 $\pm$ 0.7	1.35 $\pm$ 0.03	13.4 $\pm$ 0.4	0.97 $\pm$ 0.00	23	8.6 $\pm$ 2.3	1.3 $\pm$ 0.07	14.4 $\pm$ 1.2	0.94 $\pm$ 0.02	3.28 $\pm$ 0.22
	30	9.1 $\pm$ 0.5	1.34 $\pm$ 0.03	15.1 $\pm$ 0.4	0.96 $\pm$ 0.01	30	9.5 $\pm$ 0.0	1.28 $\pm$ 0.04	14.8 $\pm$ 0.8	0.95 $\pm$ 0.02	3.54 $\pm$ 0.18
	30 <sup>e</sup>	9.8 $\pm$ 0.2	1.30 $\pm$ 0.007	14.5 $\pm$ 0.1	0.95 $\pm$ 0.006						
DPPG	30	9.3 $\pm$ 0.4	1.43 $\pm$ 0.01	17.9 $\pm$ 0.2	0.98 $\pm$ 0.01	30	9.5 $\pm$ 1.4	1.44 $\pm$ 0.17	17.8 $\pm$ 0.7	0.96 $\pm$ 0.01	3.31 $\pm$ 0.17
DPTAP	30	5.2 $\pm$ 1.1	1.33 $\pm$ 0.06	15.3 $\pm$ 0.5	0.93 $\pm$ 0.01	30	5.2 $\pm$ 0.8	1.32 $\pm$ 0.05	15.8 $\pm$ 1.5	0.96 $\pm$ 0.02	3.58 $\pm$ 0.12

<sup>a</sup>Electron density normalized by the electron density of water,  $\rho_{\text{water}} = 0.334 \text{ e/Å}^3$ .

<sup>b</sup>Root mean square of the roughness of the interface.

<sup>c</sup>The first value represents  $\sigma_{\text{A}\beta\text{-subphase}}$  and the second value represents  $\sigma_{\text{A}\beta\text{-air}}$ .

<sup>d</sup>Parameter was fixed during refinement.

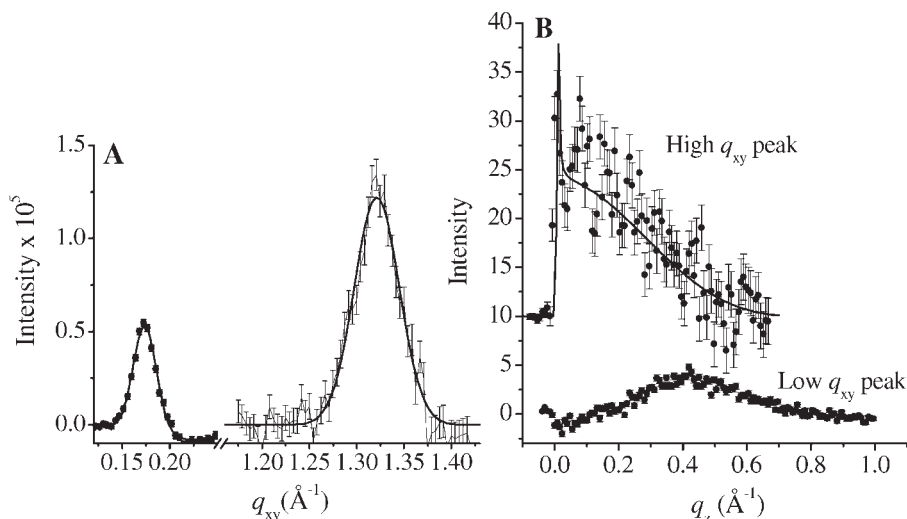
<sup>e</sup>Parameters at this pressure were obtained from a nonlinear least-square regression method.

$\beta$ -sheet formation in A $\beta$ 40 has also been provided by Maltseva and Brezesinski,<sup>59,60</sup> where infrared reflection absorption spectroscopy was used to measure the secondary structures of the peptide adsorbed at the air–water interface. From the FWHM( $q_{xy}$ ) values, in-plane coherence lengths, or the average distance over which order in the diffracting crystallites propagates, of the 4.76 and 36.2 Å  $d$ -spacing peaks were calculated to be 102 and 207 Å, respectively (Table II). Thus, the diffracting crystallites that gave rise to the 4.76 Å peak were comprised of  $\sim 20$  A $\beta$  peptides assembled in the  $\beta$ -sheet conformation, where the  $\beta$ -sheets are likely oriented parallel to the air–water interface.<sup>60</sup> Although the exact shape of the one-dimensionally aligned structure cannot be extrapolated from the present X-ray scattering data, it likely constitutes an A $\beta$  protofibril. On the other hand, the structural origin of the feature that gave rise to the 36.2 Å  $d$ -spacing is unclear. However, one can envision a type of supramolecular structure made up by the already aligned A $\beta$  peptides discussed above. Since the coherence length of this low- $q_{xy}$  peak is 207 Å, the 36.2 Å  $d$ -spacing observed could therefore be the result of  $\sim 5$  of the one-dimensionally aligned A $\beta$  peptide structures, in other words, laterally associated protofibrils, with the observed  $d$ -spacing signifying the length scale of the 1D structure in the direction perpendicular to the inter- $\beta$ -strand spacing. The integrated intensity ( $I$ ) of a Bragg peak is proportional to the number of ordered domains that scatter in the foot print of the X-ray beam. The ratio of  $I$  for the two peaks,  $I(1.33 \text{ Å}^{-1})/I(0.17 \text{ Å}^{-1})$ , was  $\sim 4$ , and provides the lower bound of the ratio between the scattering units giving rise to the two peaks.

The GIXD data of A $\beta$  adsorbed to the air-subphase interface from a PBS subphase showed no peak at 0.17 Å<sup>−1</sup> and a smaller peak at 1.33 Å<sup>−1</sup> (data not shown). Increasing the pH from 5.5 to 7.4 and the presence of salts thus prevented the larger-scale structural feature to form. This could be due to the increased net charge on the protein from approximately neutral at pH 5.5 in water to  $-3$  at pH 7.4, thereby increasing peptide–peptide electrostatic repulsion and reducing lateral assembly of the protofibrils.

Bragg rod profiles of the two A $\beta$  Bragg peaks are shown in Figure 3(B). The Bragg rod profile of the high- $q_{xy}$  peak (1.33 Å<sup>−1</sup>) has a maximum at  $q_z \sim 0 \text{ Å}^{-1}$  [Fig. 3(B)]. For phospholipids, this could be interpreted as a hexagonal unit cell with untilted tails. The same assessment, however, could not be made for the A $\beta$  film because the shape A $\beta$  adopts at the air–water interface is unclear. From the FWHM( $q_z$ ) of the Bragg rod profile for the low  $q_{xy}$  peak, the length of the A $\beta$  peptide that scattered coherently was found to be  $13 \pm 5 \text{ Å}$ . This value was less than the total peptide thickness of 18.6 Å adsorbed at the interface, indicating that while A $\beta$  adopted ordered structures, a portion of the peptide remained disordered.



**Figure 3**

Bragg peaks (A) and Bragg rod profiles (B) from GIXD data of A $\beta$  in water adsorbed to the air-water interface at 30°C. Solid lines correspond to model fits. Bragg rod profiles for the two Bragg peaks have been vertically offset for clarity.

### A $\beta$ association with DPPC monolayers

XR data for DPPC monolayers at 23 and 30 mN/m on both water and PBS were collected; fitting parameters are summarized in Table I. Pure DPPC monolayers on water and PBS were fit with the simplest two-slab model, one slab for the headgroup and one slab for the tail group, with a single interfacial roughness parameter (Table I and Fig. 4).<sup>52</sup> During the refinement of the fit, the number of electrons in the tail region was set to 242 (calculated from the chemical structure for DPPC) and the area per molecule was set to be the measured value to reduce the number of fitting parameters. The fitted reflectivity of DPPC on water showed deviations from the measured reflectivity at high  $q_z$  values ( $q_z/q_c > 26$ ) [Fig. 4(A), solid line], which could stem from the inhomogeneity of the electron density of the large headgroup [Fig. 1(B)], where a constant  $\rho$  value, or a single slab, to model the headgroup might be inadequate. However, when a three-slab model was used, fitting became over-parameterized. Two additional fitting techniques, nonlinear regression and a model independent technique, were also used to fit the reflectivity data. Neither method significantly improved fitting of the high  $q_z/q_c$  data. The dashed line in Figure 4(A) shows the best fit to the reflectivity data using a nonlinear least square regression method with a Levenberg-Marquardt minimization algorithm.<sup>61</sup> The fit showed improvements in the first minimum and maximum of the reflectivity curve compared with the two-slab model fit; fitting parameters are summarized in Table I. As shown, fitting parameters were close to those obtained from the two-slab model.

The improved fit gave smaller errors for both roughness and length parameters.

A $\beta$  did not insert into DPPC monolayers at a bilayer equivalent pressure of 30 mN/m on water or PBS<sup>32</sup> and no detectable changes in  $R/R_F$  with the addition of A $\beta$  were observed compared with those of the lipid alone (data not shown). At a lower pressure of 23 mN/m, A $\beta$  inserted into the DPPC monolayer, resulting in  $\Delta A/A$  of 4 and 6% on water and PBS subphase, respectively (Table III).<sup>32</sup> XR profile of DPPC on water after A $\beta$  injection was identical to that of DPPC alone at 23 mN/m (data not shown). On the PBS subphase, however, injection of A $\beta$  induced small changes in the XR profile of DPPC at 23 mN/m [Fig. 4(B)]. Fitting of the XR data yielded two slabs with  $\rho$  and  $L$  values nearly identical to that of the pure lipid film and an additional slab with a  $\rho$  that was slightly higher than that of water [Fig. 4(B'), Tables I and III]. These results indicate that a diffuse layer (or low concentration) of A $\beta$  was adsorbed underneath the DPPC monolayer at 23 mN/m and 30°C on PBS.

The Bragg peaks and Bragg rod profiles of DPPC at 30 mN/m on water and PBS are shown in Figure 5(A,B). At 23 mN/m, DPPC was just below its phase transition pressure and no in-plane ordering was detected. At 30 mN/m and 30°C on a water subphase, two Bragg peaks at  $q_{xy} = 1.38$  and  $1.46 \text{ \AA}^{-1}$  [Fig. 5(A), filled squares] were resolvable, indicative of a distorted hexagonal (or centered rectangular) unit cell. When compressed to 30 mN/m at 15°C, DPPC has been shown to give rise to three resolvable Bragg peaks, indicative of oblique packing

**Table II**Parameters Obtained from GIXD Data of A $\beta$ , Single Component Lipids, and A $\beta$ -Lipid Films at the Air-Subphase Interface at 30°C

		In-plane Bragg peaks				Out-of-plane Bragg rods					
			<i>d</i> -Spacing unit cell <i>a</i> , <i>b</i> (Å)	$\gamma$ (°)	Coherence length <i>L</i> <sub>C</sub> (Å)	Area per molecule (Å <sup>2</sup> ) <sup>c</sup>	Coherence length <i>L</i> <sub>C</sub> (Å)	Tilt direction	Tilt angle <i>t</i> (°)	$\sigma$ (Å)	$\chi^2$
Sample	$\pi$ (mN/m)										
Water subphase											
A $\beta$	12	Peak 1	36.2	207	1511 <sup>a</sup>						
		Peak 2	4.76	102	26.1 <sup>a</sup>						
DPPC	23		No in-plane diffraction								
	30		5.07	116	242, 47.5	23.1	14.0 $\pm$ 1.1	NN	27	1.1 $\pm$ 0.1	4.2
DPPG	30		4.83	120	598	20.2	16.4 $\pm$ 2.8	NN	4	2.16 $\pm$ 1.2	19.3
DPTAP	30		5.06	116	415, 90.3	23.1	14.6 $\pm$ 0.3	NN	28	1.14 $\pm$ 0.04	3.7
A $\beta$ + DPPC	23		No in-plane diffraction								
	30		5.13	115	240, 78.4	23.9	14.0 $\pm$ 1.1	NN	27	1.1 $\pm$ 0.1	4.2
A $\beta$ + DPPG	30	Peak 1	4.94	119	249, 109	21.3	15.1 $\pm$ 0.3	NN	17	0.4 $\pm$ 0.3	11
		A $\beta$ Peak	4.76	120	478	26.1	11.8 $\pm$ 2.4				1.4
A $\beta$ + DPTAP	30		4.98	118	276, 96.9	21.9	15.5 $\pm$ 0.4	NN	18	1.61 $\pm$ 0.23	3.0
PBS subphase											
A $\beta$	15		No in-plane diffraction								
DPPC	23		5.09	115	339, 58.7	23.6	13.7 $\pm$ 0.4	NN	28	0.72 $\pm$ 0.08	4.2
	30		5.05	116	372, 81.8	22.9	13.6 $\pm$ 0.9	NN	30	0.90 $\pm$ 0.30	7.0
DPPG	30		4.88	119	518, 112	20.9	15.7 $\pm$ 2.7	NN	14	2.5 $\pm$ 0.4	7.1
DPTAP	30		5.01	117	359, 77.0	22.5	15.0 $\pm$ 0.3	NN	22	0.3 $\pm$ 1.4	3.1
A $\beta$ + DPPC	23		5.07	117	375, 62.1	23.3	14.8 $\pm$ 0.4	NN	26	0.4 $\pm$ 0.19	5.7
	30		5.06	116	384, 66.3	23.1	13.6 $\pm$ 0.9	NN	30	0.9 $\pm$ 0.3	7.0
A $\beta$ + DPPG	30		4.90	119	555, 171	21.0	15.2 $\pm$ 3.1	NN	14	2.1 $\pm$ 1.0	9.2
A $\beta$ + DPTAP	30		5.05	116	540, 148	22.9	10.3 $\pm$ 2.7	NN	22	0.5 <sup>b</sup>	7.2

<sup>a</sup>Values calculated assuming a hexagonal packing to estimate the area occupied by each A $\beta$  at the air-water interface.<sup>b</sup>Parameter was fixed during refinement.<sup>c</sup>For the phospholipids, area per molecule indicates area per one acyl tail.

of acyl chains.<sup>62</sup> At 30°C the *d*-spacings of the DPPC Bragg peaks in Figure 5(A) were  $d_{11} = 4.56$  Å and  $d_{02} = 4.29$  Å, corresponding to a rectangular unit cell with dimensions  $a_r = 5.39$  Å,  $b_r = 8.58$  Å, and  $\gamma = 90^\circ$ . In the distorted hexagonal packing representation, the dimensions of the unit cell were  $a_h = b_h = 5.07$  Å and  $\gamma = 116^\circ$ , where  $a_h$  and  $b_h$  are the magnitude of the unit cell vector and  $\gamma$  is the angle between the base vectors of the unit cell (Table II). Analysis of the Bragg rod profile [Fig. 5(B), filled squares] showed that the hydrocarbon tails of DPPC were tilted by  $27^\circ$  from the surface normal. The tilt (azimuthal angle) was  $19^\circ$  from nearest neighbor direction of  $a_h + b_h$  (vectors) (Table II). Addition of A $\beta$  resulted in small changes in the unit cell dimensions as evident by the shift towards the smaller  $q_{xy}$  values of the first, broad, Bragg peak [Fig. 5(A), open squares] and significant decreases of the integrated intensities of the diffraction peaks indicated a decrease in the amount of ordered material in the footprint of the beam. On PBS, a third Bragg peak was resolvable for DPPC at 30 mN/m [arrow in Fig. 5(A)]. The three peaks arise from an oblique unit cell, where  $a_h \neq b_h$  and  $\gamma \neq 120^\circ$ . With the addition of A $\beta$ , the third peak was no longer discernable [Fig. 5(A), open triangles]. Overall, the presence of A $\beta$  in the subphase did not result in significant changes

in the lateral ordering of the DPPC film for all pressures (23 and 30 mN/m) and subphase conditions tested.

### A $\beta$ association with DPPG monolayers

XR data and fit of DPPG at 30 mN/m and 30°C on water and PBS are shown in Figure 6(A,B); the corresponding  $\rho(z)$  profiles are shown in Figure 6(A', filled circles) and (B', filled triangles). Fitting of XR data on both water and PBS yielded similar  $\rho(z)$  profiles; the headgroup thicknesses on water and PBS were 9.3 and 9.5 Å and the tail group thicknesses on water and PBS were 17.9 and 17.8 Å (Table I), giving rise to total lipid thicknesses on water and PBS of 27.2 and 27.3 Å, respectively.  $\rho/\rho_{\text{water}}$  values of the headgroup and tail group on both subphase conditions were  $\sim 1.4$  and 0.97, respectively.

A $\beta$  spontaneously inserted into DPPG at 30 mN/m and 30°C on water, with a  $\Delta A/A$  of 14%. On PBS, however, the electrostatic repulsion between the overall negatively charged A $\beta$  and the negatively charged lipid head groups resulted in negligible insertion, with a  $\Delta A/A$  of less than 2% (Table III).<sup>32</sup> It is thus not surprising that with the addition of A $\beta$ , the  $R/R_F$  did not change significantly for DPPG at 30 mN/m on PBS (data not shown). On a water subphase, however, a reproducible shoulder

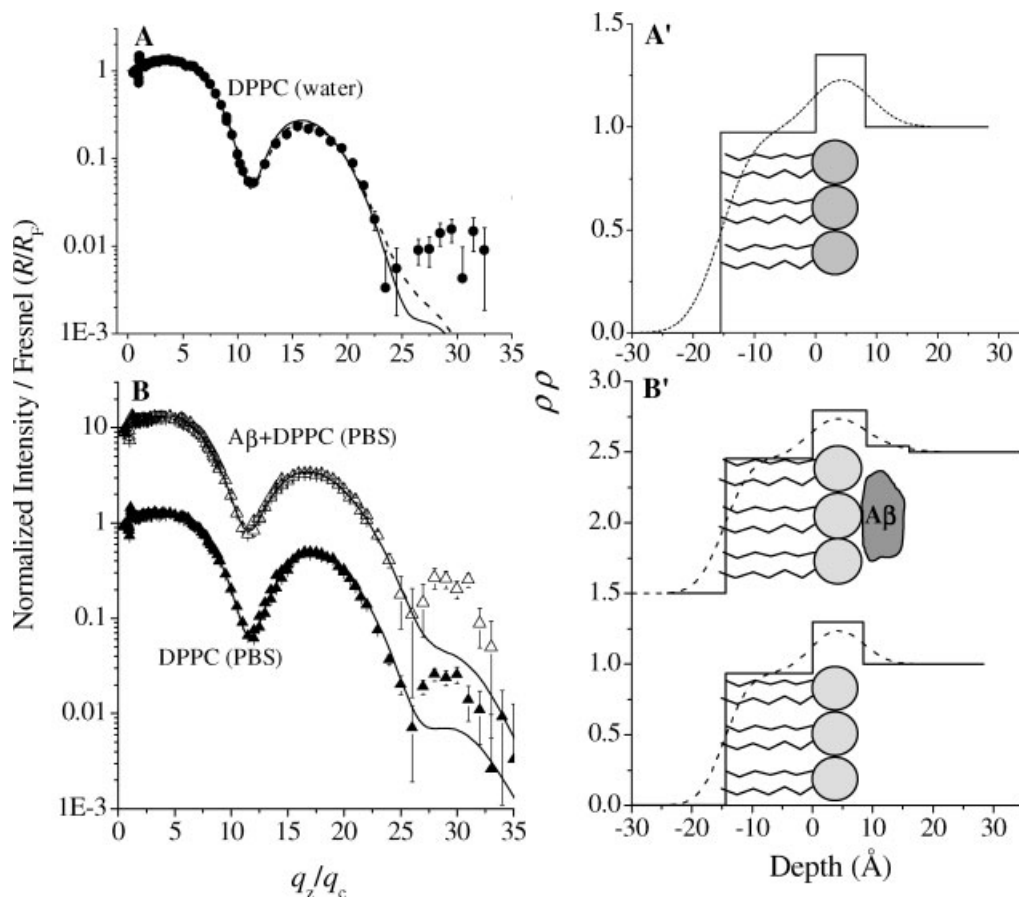


**Figure 4**

XR data and fit for DPPC on water at 23 mN/m (A, ●), DPPC on PBS at 23 mN/m before (▲) and after (Δ) Aβ addition at 30°C (B). The solid lines represent fitted reflectivity curves from slab models. Dashed line in A represents fitted reflectivity from a nonlinear least-square regression method. Corresponding electron density profiles of DPPC on water (A') and on PBS before and after Aβ addition (B') obtained from fitting XR data. Both unsmear (solid line) and smeared (dotted line) electron density profiles are plotted. Schematics of the different molecular slabs that gave rise to the electron density profiles have been vertically offset for clarity.

appeared on the second hump of the reflectivity profile [arrow in Fig. 6(A)]. Fitting  $R/R_F$  with a two-, three-, or four-slab model did not yield acceptable fits. Fitting using a five-slab model provided satisfactory results. However, the five-slab model introduced 11 parameters ( $\rho$  and  $L$  for each slab plus  $\sigma$ ) and the fitting became over-parameterized. To resolve the problem, two constraints were used. The insertion of Aβ resulted in an area increase of 14% per DPPG molecule; we therefore constrained the electron densities of the tail group (slab 5) and headgroup with inserted Aβ (slab 3) to be the weighted averages between DPPG and Aβ. Specifically,  $\rho_S/\rho_{\text{water}}$  was set to be 0.83 (a weighted average of  $\rho_{\text{tail}}/\rho_{\text{water}} = 0.97$  and  $\rho_{\text{air}}/\rho_{\text{water}} = 0$ ) and  $\rho_3/\rho_{\text{water}}$  was set to be 1.40 (a weighted average of  $\rho_{\text{head}}/\rho_{\text{water}} = 1.44$  and  $\rho_{\text{A}\beta}/\rho_{\text{water}} = 1.26$ ). The  $\rho(z)$  profile obtained using the constraints is shown in Figure 6(A'), along with a sche-

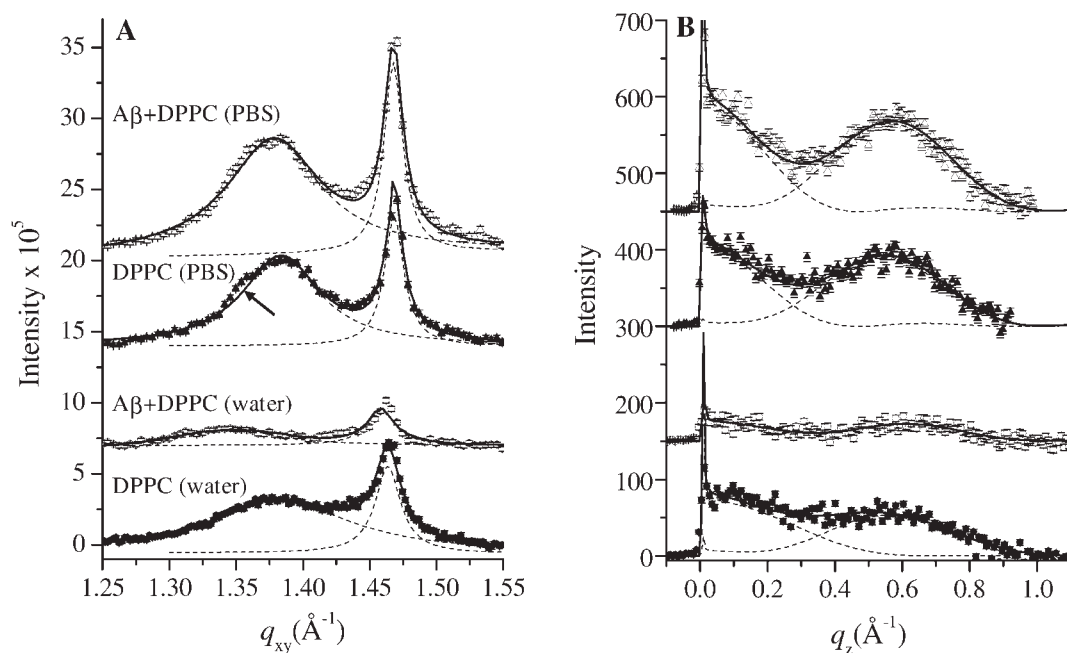
matic depicting the molecular composition of each layer. As shown, in addition to being adsorbed underneath the DPPG monolayer, Aβ also penetrated into the lipid monolayer, with a portion of the peptide associating with the hydrophobic tail groups. The resulting total thickness of 39.6 Å of the Aβ layer (adding slabs 1–4) was roughly two times the thickness of pure Aβ adsorbed to the air–water interface, indicating that multiple layers of Aβ were associated with the DPPG monolayer on water.

The Bragg peaks and corresponding Bragg rod profiles of DPPG in water and PBS at 30 mN/m are shown in Figure 7. Pure DPPG on water showed a single Bragg peak at  $q_{xy} = 1.50 \text{ Å}^{-1}$  with  $\text{FWHM} = 0.013 \text{ Å}^{-1}$  [Fig. 7(A), filled circles], indicative of a hexagonal unit cell with a six-fold degeneracy where the three scattering planes of the unit cell had identical  $d$ -spacings. The lattice dimensions of the ordered lipid tails were  $a_h = b_h = 4.83 \text{ Å}$ ,

**Table III**  
Fitting Parameters for XR Data of A $\beta$ -Lipid Films at the Air-Subphase Interface at 30°C

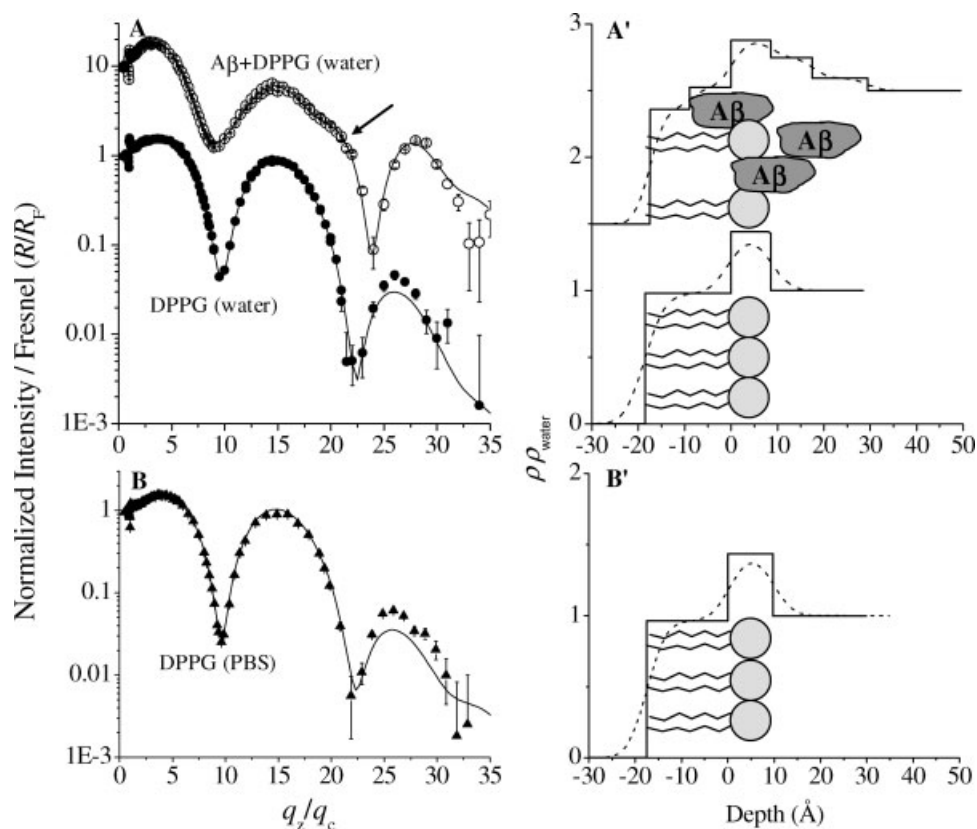
Sample	$\pi$ (mN/m)	Insertion $\Delta A/A$ (%) <sup>a</sup>	Subphase/Air									
			Thickness $L_1$ (Å)	$\rho_1/\rho_{\text{water}}$	Thickness $L_2$ (Å)	$\rho_2/\rho_{\text{water}}$	Thickness $L_3$ (Å)	$\rho_3/\rho_{\text{water}}$	Thickness $L_4$ (Å)	$\rho_4/\rho_{\text{water}}$	Thickness $L_5$ (Å)	$\rho_5/\rho_{\text{water}}$
Water subphase												
A $\beta$ + DPPC	23	4	6.5 $\pm$ 0.3	1.36 $\pm$ 0.01	14.0 $\pm$ 0.1	0.93 $\pm$ 0.00						3.61 <sup>c</sup>
A $\beta$ + DPPG	30	14	11.8 $\pm$ 0.3	1.09 $\pm$ 0.00	9.1 $\pm$ 0.3	1.25 $\pm$ 0.00	8.3 $\pm$ 0.5	1.38 $\pm$ 0.1	10.3 $\pm$ 0.9	0.99 $\pm$ 0.01	7.3 $\pm$ 0.8	0.8 $\pm$ 0.04
A $\beta$ + DPTAP	30	35	12.7 $\pm$ 0.5	1.32 $\pm$ 0.01	12.6 $\pm$ 0.1	0.56 $\pm$ 0.03						
PBS subphase												
A $\beta$ + DPPC	23	6	7.3 $\pm$ 2.8	1.04 $\pm$ 0.03	8.9 $\pm$ 0.9	1.29 $\pm$ 0.01	14.1 $\pm$ 0.2	0.95 $\pm$ 0.01				3.46 $\pm$ 0.06
A $\beta$ + DPPG	30	<2	9.5 $\pm$ 1.2	1.44 $\pm$ 0.05	17.8 $\pm$ 0.7	0.96 $\pm$ 0.01						3.31 $\pm$ 0.07
A $\beta$ + DPTAP	30	4	11.7 $\pm$ 5.0	1.04 $\pm$ 0.01	4.7 $\pm$ 2.0	1.29 $\pm$ 0.17	15.3 $\pm$ 1.7	0.96 $\pm$ 0.02				6.3 $\pm$ 5.3 3.37 $\pm$ 1.53
												3.78 $\pm$ 0.51 3.58 $\pm$ 0.16 <sup>e</sup>





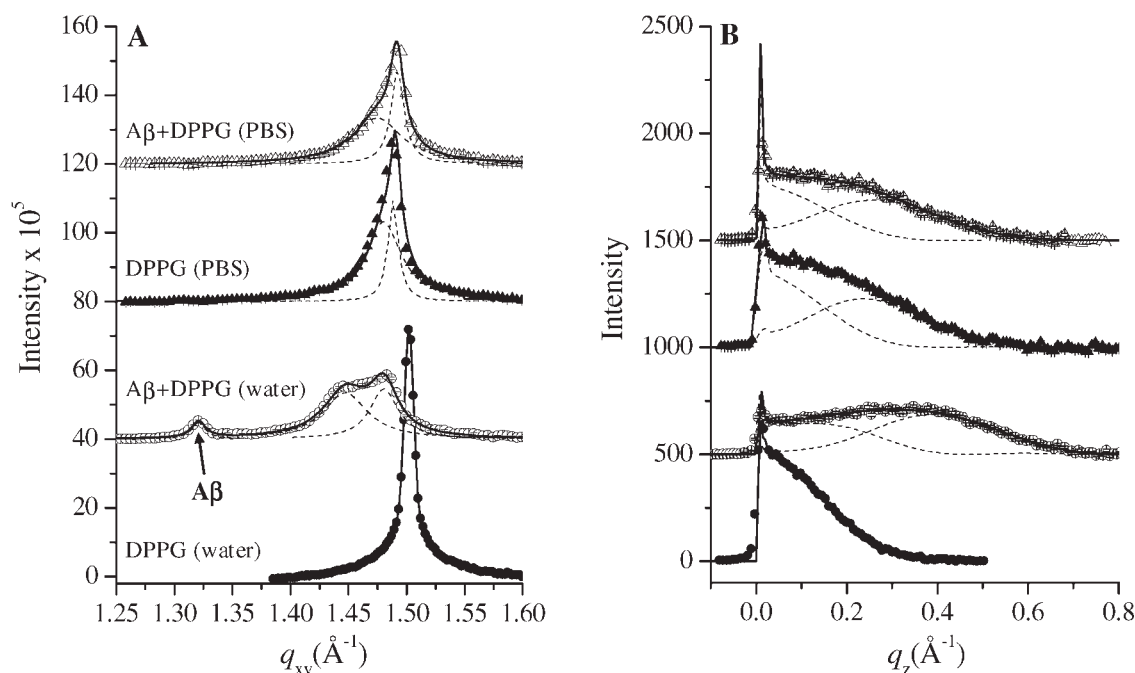
**Figure 5**

Bragg peaks (A) and Bragg rod profiles (B) from GIXD data of DPPC on water at 30 mN/m before (●) and after (○) A $\beta$  addition and DPPC on PBS at 30 mN/m before (▲) and after (△) A $\beta$  addition at 30°C. Dashed lines are fits of individual peaks and the solid lines correspond to the overall fit. Data have been vertically offset for clarity.



**Figure 6**

XR data and fit for DPPG on water at 30 mN/m before (●) and after (○) A $\beta$  addition (A) and DPPG on PBS at 30 mN/m (B, ▲) at 30°C. The solid lines represent fitted reflectivity curves. Corresponding electron density profiles of DPPG monolayer on water before and after A $\beta$  addition (A') and on PBS without A $\beta$  (B') obtained fitting XR data. Both unsmeared (solid line) and smeared (dotted line) electron density profiles were plotted. Schematics of the different molecular slabs that gave rise to the electron density profiles were also included (A' and B'). XR data and electron density profiles have been vertically offset for clarity.

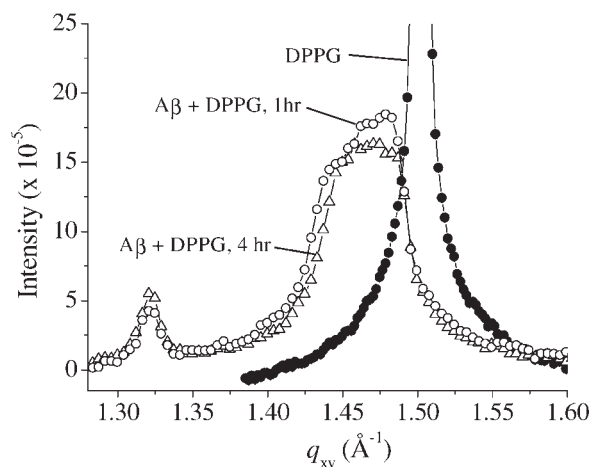
**Figure 7**

Bragg peaks (A) and Bragg rod profiles (B) from GIXD data of DPPG on water at 30 mN/m (●), A $\beta$  associated with DPPG on water at 30 mN/m (○), DPPG on PBS at 30 mN/m (▲), and A $\beta$  associated with DPPG on PBS at 30 mN/m (△) at 30°C. Dashed lines are fits of individual peaks and the solid lines correspond to the overall fit. Arrow indicates the in-plane diffraction peak that arose from the ordering of A $\beta$ . Data have been vertically offset for clarity.

The injection of A $\beta$  into the subphase of the DPTAP monolayer on water resulted in a  $\Delta A/A$  of 35% (Table III).<sup>32</sup> The XR profile for the lipid film could still be fit by two slabs [Fig. 9(A, open circles) and (A', top)]. However, the slab parameters were different from those of the pure lipid.  $\rho_2$  (slab at the air interface) was lower than  $\rho_{\text{tail}}$ , the  $L_1$  (slab at the water interface) was larger than  $L_{\text{head}}$ , and the  $\sigma$  value was larger than that of pure DPTAP (Tables I and III). These parameters indicated that the lipid tails (slab 2) were at a lower packing density (due to A $\beta$  insertion) than that of pure lipid and the thick slab at the water interface (slab 1) encompassed lipid headgroups and inserted peptides with part of the peptide protruding into the subphase [schematic in Fig. 9(A')]. Because of the similarity between  $\rho_{\text{A}\beta}$  and  $\rho_{\text{head,DPTAP}}$  values (Table I), a single slab representing head/A $\beta$  and A $\beta$  underneath the monolayer yielded the best result in fitting the XR data with a larger  $\sigma$ , stemming from the more inhomogeneous and diffuse slab.

In PBS, where there was strong charge–charge attraction between the negatively charged A $\beta$  and positively charged lipid headgroups, the addition of A $\beta$  resulted in a  $\Delta A/A$  of only 4% (Table III).<sup>32</sup> The low insertion resulted from XR data of A $\beta$  associated with the DPTAP monolayer was best-fit with a three-slab model [Fig. 9(B, open triangles) and (B', top)]. Slab 1, which was underneath the DPTAP monolayer and had a  $\rho$ -value that was slightly higher than

$\rho_{\text{water}}$  was composed of a diffuse layer of A $\beta$ . Slabs 2 and 3 were almost identical to those of the pure DPTAP monolayer, representing the headgroup and tail groups, respectively.  $\rho_2$  was slightly lower than  $\rho_{\text{head}}$  of pure

**Figure 8**

Temporal evolution of the Bragg peaks for DPPG at 30 mN/m and 30°C before (●) and 1 (○) and 4 h (△) after the addition of A $\beta$ . For clarity, the error bars of the GIXD data taken after A $\beta$  addition are not shown.

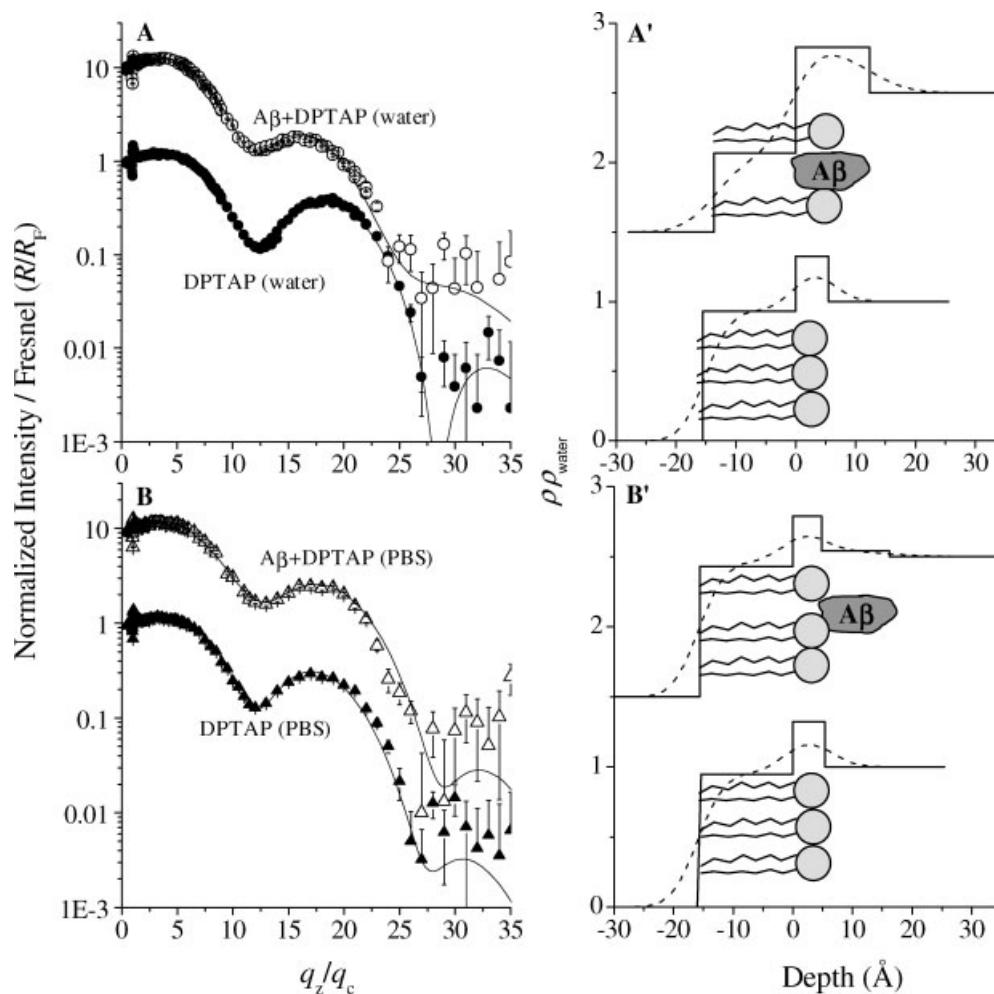


**Figure 9**

XR data and fit for DPTAP on water at 30 mN/m before (●) and after (○) Aβ addition (A) and DPTAP on PBS at 30 mN/m before (▲) and after (Δ) Aβ addition (B) at 30°C. The solid lines represent fitted reflectivity curves. Corresponding electron density profiles of DPTAP monolayer on water with and without Aβ (A') and on PBS with and without Aβ (B') obtained fitting XR data. Both unsmeared (solid line) and smeared (dotted line) electron density profiles were plotted. Schematics of the different molecular slabs that gave rise to the electron density profiles were also included (A' and B'). XR data and electron density profiles have been vertically offset for clarity.

DPTAP, indicating that a small fraction of the peptide may be inserted into the headgroup region [Fig. 9(B')].

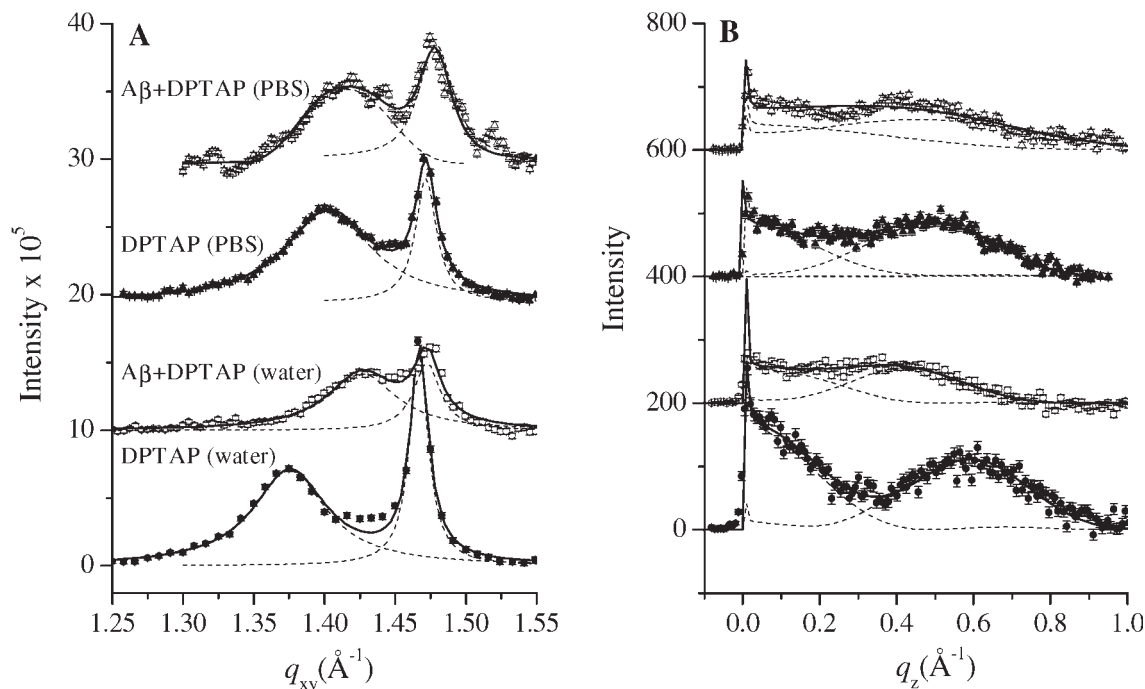
The Bragg peaks and the corresponding Bragg rod profiles of DPTAP on water and PBS are shown in Figure 10(A,B). For both subphase conditions, pure DPTAP gave rise to two Bragg peaks, indicating a distorted hexagonal cell with  $a_h = b_h = 5.06$  Å,  $\gamma = 116^\circ$ , and  $A = 23.1$  Å<sup>2</sup> for water, and  $a_h = b_h = 5.01$  Å,  $\gamma = 117^\circ$ , and  $A = 22.5$  Å<sup>2</sup> for PBS. The analysis of the Bragg rod profiles showed that the hydrocarbon tails of DPTAP lipids were tilted by 28 and 22° on water and PBS, respectively.

Contrary to the unit cell expansion found during the association of Aβ to a DPPG monolayer on water, the association of Aβ to DPTAP caused a contraction of the DPTAP unit cell, where the Bragg peak shifted to a

higher  $q_{xy}$  value [Fig. 10(A), open squares], yielding unit cell dimensions of  $a_h = b_h = 4.98$  Å,  $\gamma = 118^\circ$ , and  $A = 21.9$  Å<sup>2</sup> (Table II). A decrease in the total integrated intensities of the Bragg peaks was also observed. Aβ association also significantly reduced the tilt angle of the DPTAP tails, from 28 to 18°. On PBS, the injection of Aβ also caused a contraction of the DPTAP unit cell. However, the change was smaller compared with that observed on water.

#### Aβ association with binary DPPC-PA monolayers

To determine whether the ordered Aβ peak induced by DPPG was a lipid-specific effect, we used binary lipid

**Figure 10**

Bragg peaks (A) and Bragg rod profiles (B) from GLXD data of DPTAP on water at 30 mN/m before (●) and after (○) A $\beta$  addition and DPTAP on PBS at 30 mN/m before (▲) and after (△) A $\beta$  addition at 30°C. Dashed lines are fits of individual peaks and the solid lines correspond to the overall fit. Data have been vertically offset for clarity.

monolayers composed of 1:1 (by mole) and 1:2 DPPC and the negatively charged PA to mimic a DPPG monolayer, providing different packing and charge density in the film. The observed Bragg peaks of the two mixtures are shown in Figure 11(A). The 1:1 mixture gave rise to two peaks, indicative of a distorted hexagonal unit cell. With the injection of A $\beta$ , no insertion was observed; the unit cell dimensions of the lipids did not change and no ordered A $\beta$  peak was detected [Fig. 11(A)]. The 1:2 DPPC:PA mixture gave rise to a single Bragg peak, indicative of hexagonal packing. The location of the peak was almost identical to the location of the DPPG peak on water (Table II), signifying that the 1:2 mixture was a good mimic of DPPG in terms of unit cell dimensions. However, the binary lipid mixture did not induce any ordering of A $\beta$ . No significant differences in Bragg rod profiles and the total integrated intensity were observed before and after injecting A $\beta$  for both binary lipid mixtures [Fig. 11(B)].

### Neutron reflectivity

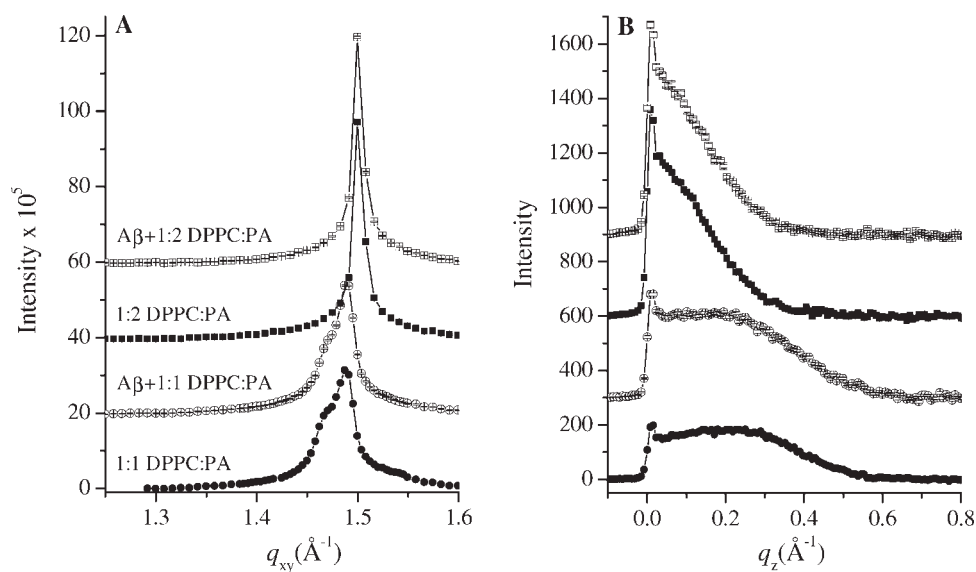
NR measurements were made for tail-deuterated DPPG (d62-DPPG) monolayer at the air-D<sub>2</sub>O interface before and after A $\beta$  injection. The experimentally measured reflectivity profiles and fits for d62-DPPG at 30

mN/m and 30°C on D<sub>2</sub>O before and after peptide injection are shown in Figure 12(A); the corresponding SLD profiles are shown in Figure 12(B). The error bars on the data represent the statistical errors of the measurement and the uncertainty in the  $q_z$  resolution and were nearly constant in the measured range.

A two-slab model yielded an excellent fit of the NR data of d62-DPPG [Fig. 12(A), filled circles], with the first slab representing portions of the lipid headgroup nearest to the subphase and the second slab representing the deuterated tail group and the carboxylic ester groups on the lipid headgroup. The thickness values of the tail group and headgroup were larger and smaller (Tables IV and I), respectively, compared with those obtained from XR because the designation of the slabs was different. For NR, the carboxylic esters exhibit SLD similar to the deuterated tail groups and were included in the tail group slab, whereas for XR, the carboxylic esters were included as a part of the headgroup. The overall thickness of d62-DPPG obtained from NR was 26.5 Å, which is in good agreement with the overall thickness of 27.2 Å obtained from XR.

With the injection of A $\beta$ , the NR of d62-DPPG changed significantly [Fig. 12(A), open circles]. A two-slab model still produced an excellent fit to the data. However, the first slab became a combination of peptide

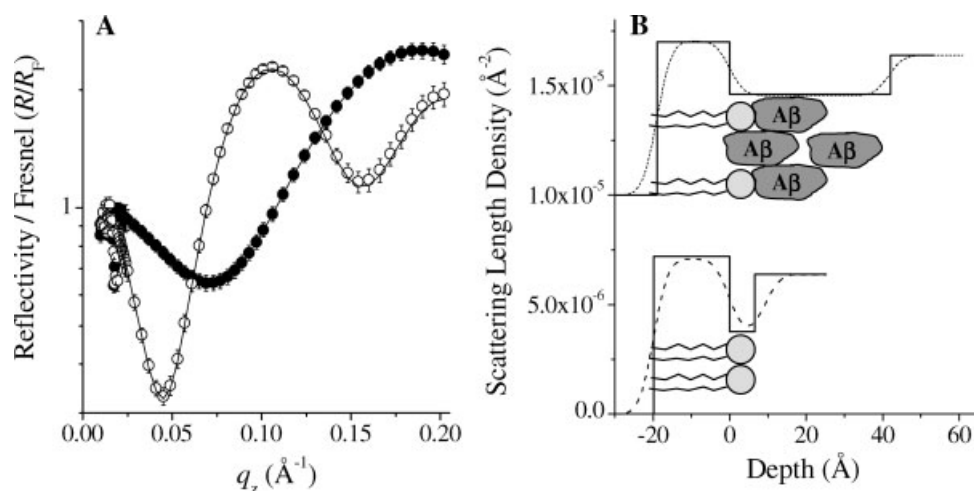


**Figure 11**

Bragg peaks (A) and Bragg rod profiles (B) from GLXD data of 1:1 DPPC:PA on water at 30 mN/m before (●) and after (○)  $A\beta$  addition and 1:2 DPPC:PA on water at 30 mN/m before (■) and after (□)  $A\beta$  addition at 30°C. Data have been vertically offset for clarity.

adsorbed underneath the monolayer and peptide partially inserted into the monolayer [Fig. 12(B), top]. The SLD of this layer was slightly larger than that of the lipid headgroup (Table IV) because the peptide brought with itself  $D_2O$  molecules as it inserted into the headgroup region.<sup>63</sup> We note that the thickness obtained for the peptide layer (41.5 Å) was in good agreement with the

result from XR measurements [39.6 Å, Fig. 6(B)]. The SLD for the tail group was slightly smaller, by 3%, compared with that of pure lipid, indicating that the insertion of the peptide into the tail region was less than expected based on insertion results. This could be partly due to the differences in the phase behaviors between deuterated and undeuterated lipids,<sup>64</sup> which in turn can

**Figure 12**

NR data and fit for deuterated d62-DPPG on water at 30 mN/m before (●) and after (○)  $A\beta$  addition at 30°C (A). Corresponding SLD profiles of d62-DPPG at 30 mN/m on water before and after  $A\beta$  addition (B). Both unsmeared (solid line) and smeared (dotted line) SLD profiles were plotted. Schematics of the different molecular slabs that gave rise to the SLD profiles were also included (B). SLD profiles have been vertically offset for clarity.

**Table IV**Fitting Parameters for Neutron Reflectivity Data of A $\beta$ -DPPG Films at the Air-D<sub>2</sub>O Interface at 30°C

Sample	$\pi$ (mN/m)	Headgroup region		Tail region		$\sigma$ (Å) <sup>b</sup>	$\chi^2$
		Thickness $L_h$ (Å)	$\rho_h^a$	Thickness $L_t$ (Å)	$\rho_t$		
d-62 DPPG	30	6.5	3.8 E-06	20	7.2 E-06	3	1.0
d-62 DPPG+A $\beta$	30	42	4.6 E-06	19	7.0 E-06	3	1.5

<sup>a</sup> $\rho$  of D<sub>2</sub>O is 6.38 E-6.<sup>b</sup>Roughness value ( $\sigma$ ) was held constant at 3 Å because fitted parameters were not sensitive to small changes in  $\sigma$  values due to a limited  $q_z$  range of 0.2 Å.

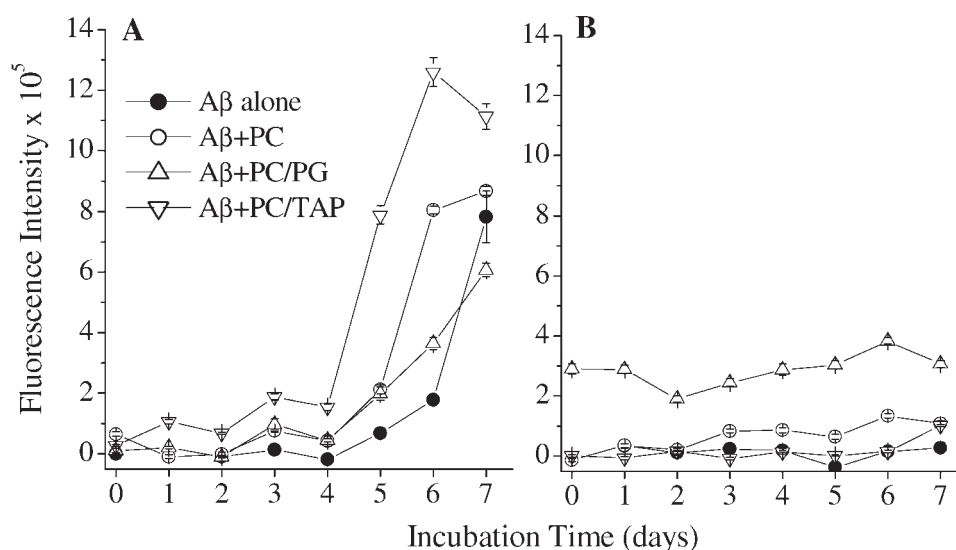
affect how A $\beta$  interacts with the tail groups. Additionally, the deuterated solvent, D<sub>2</sub>O, may also exert some effects on the insertion of A $\beta$  at the lipid interface.

### Effect of lipids on A $\beta$ fibril formation

To evaluate the effect of A $\beta$ -lipid interactions on the aggregation of A $\beta$ , 100  $\mu$ M A $\beta$  was incubated with large unilamellar vesicles (100-nm diameter) made up of either the zwitterionic lipid POPC, POPC containing 30 mol% anionic POPG, or POPC containing 30 mol% cationic DMTAP. The monounsaturated lipid POPC and POPG lipids and the 14-carbon acyl chain lipid DMTAP lipid were used instead of their saturated, 16-carbon acyl chain counterparts used in monolayer studies because they are more physiologically relevant. Additionally, these lipids have lower main transition temperatures ( $T_m$ ), so that at the incubation temperature of 25°C, the vesicles were more fluid ( $T_m$  values of the saturated lipids DPPC, DPPG, and DPTAP are 41, 41 (Avanti Polar Lipids), and

45°C,<sup>65</sup> respectively). A $\beta$ , first dissolved in DMSO at 5 mg/mL, was incubated at 100  $\mu$ M with each type of lipid vesicles in either water or PBS at 25°C. Control samples of A $\beta$  incubated alone in water and PBS were also prepared. A number of analytical techniques were used to characterize the samples. The amount of A $\beta$  adsorbed to the vesicle surface, vesicle size distribution, formation of fibrils, and the morphology of the incubated species were monitored using SE-HPLC, DLS, ThT binding fluorescence assay, and TEM, respectively.

At 100  $\mu$ M, A $\beta$  incubated alone in pH 7.4 PBS showed a lag phase of  $\sim$ 4 days, followed by large increases in ThT fluorescence, indicating a rapid fibril growth phase [Fig. 13(A), filled circles]. ThT fluorescence profiles of A $\beta$  incubated with different vesicles, at a peptide to lipid mole ratio of 1:20, exhibited the same kinetics characteristics—a lag phase followed by rapid fibril growth phase. A $\beta$  incubated with POPC or POPC/POPG vesicles yielded ThT fluorescence signal that was similar compared with that of A $\beta$  incubated alone [Fig. 13(A), open

**Figure 13**

Background subtracted ThT fluorescence emission intensity of 100  $\mu$ M A $\beta$  incubated with POPC, POPC containing 30 mol% POPG, or POPC containing 30 mol% DMTAP in either PBS (A) or water (B) at 25°C and a protein to lipid mole ratio of 1:20.

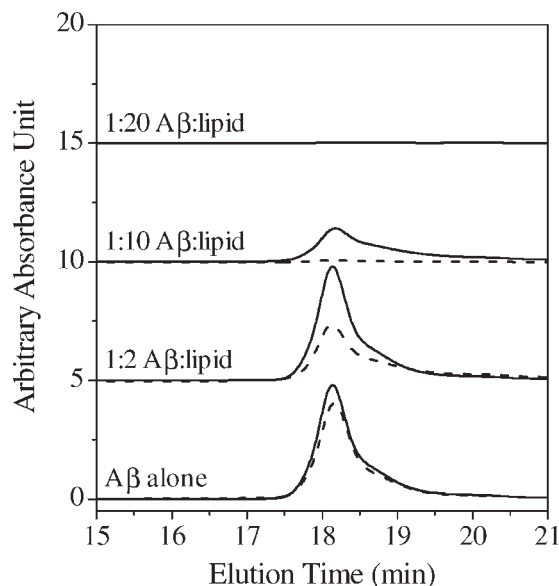


**Figure 14**

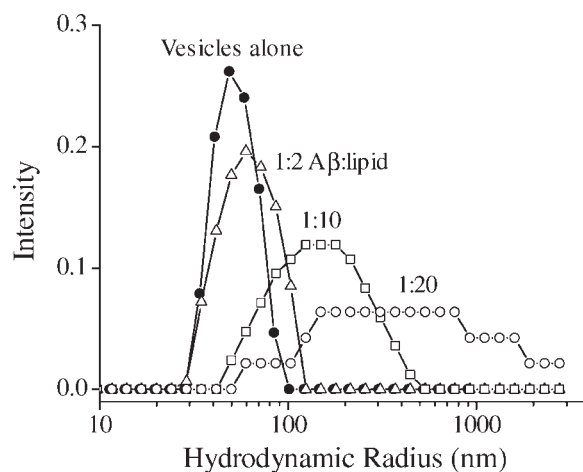
Size exclusion-HPLC chromatographs of A $\beta$  incubated with different levels of POPC vesicles containing 30 mol% POPG after 0 day (solid line) and 11 days (dashed line) of incubation at 25°C in water.

circles and open triangles]. A $\beta$  incubated with POPC/DMTAP vesicles exhibited the earliest fibril growth phase [Fig. 13(A), open inverted triangle]. This was likely due to the strong charge-charge attraction between the negatively charged A $\beta$  at pH 7.4 and the positively charged DMTAP that resulted in the adsorption of A $\beta$  to the vesicles surface, effectively increasing the local A $\beta$  concentration that led to a higher fibril nucleation rate, which was reflected in the shorter lag phase.

A $\beta$  incubated in water exhibited a much longer lag phase—no increases in ThT fluorescence was observed for up to 26 days of incubation [Figs. 13(B) and 16, filled circles]. In the presence of lipid vesicles (1:20 A $\beta$  to lipid mole ratio), ThT signal for A $\beta$  incubated with POPC and POPC/DMTAP vesicles in water remained low during 7 days of incubation [Fig. 13(B)]. No increases in ThT fluorescence were detected from these samples after 22 days of incubation (data not shown). In contrast, A $\beta$  incubated with POPC/POPG vesicles in water [Fig. 13(B), open triangle] showed an immediate increase in ThT fluorescence and the level of fluorescence stayed unchanged during 7 days of incubation. The origin of the ThT fluorescence signal from A $\beta$  incubated with POPC/POPG vesicles, however, was unclear. Since the signal increase was immediate after the addition of A $\beta$  to vesicles, it is unlikely that the signal was due to the binding of ThT to mature fibers. Moreover, the vesicles solution was observed to turn cloudy within 10 min of adding A $\beta$ , indicating that the adsorption of A $\beta$  to vesicle surface

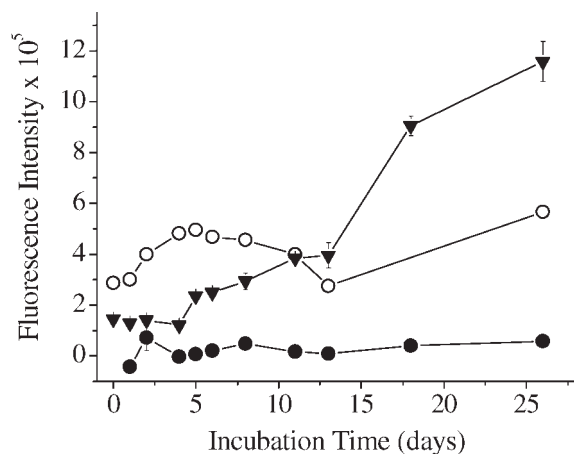
had caused the vesicles to agglomerate and precipitate. The aggregation of vesicles induced by the adsorption of a number of amyloid disease-linked peptides had been reported previously.<sup>66</sup> Analyzing the sample with SE-HPLC, after the precipitates had been removed by centrifugation, showed that no soluble A $\beta$  was left in the solution (see Fig. 14). Thus, at a protein to lipid ratio of 1:20, all A $\beta$  became associated with the POPC/POPG vesicles. The moderate increase in ThT fluorescence observed during the incubation of A $\beta$  with POPC/POPG vesicles [Fig. 13(B), unfilled triangles], therefore, was likely due to a weak binding of ThT to A $\beta$  adsorbed to vesicle surface, not due to the formation of mature fibrils. Additionally, because all A $\beta$  became associated with vesicles and precipitated out of solution, we were unable to evaluate the effect of POPC/POPG vesicle-associated A $\beta$  on A $\beta$  fibril formation.

To resolve the effect of POPC/POPG vesicles on A $\beta$  fibrillogenesis in water, A $\beta$  (100  $\mu$ M) was incubated with lower concentrations of lipids, at 1000 and 200  $\mu$ M, or at protein to lipid mole ratios of 1:10 and 1:2. Within 10 min of adding A $\beta$  to vesicles, size distribution of vesicles measured by DLS broadened and shifted to larger sizes in a lipid concentration-dependent manner (see Fig. 15). SE-HPLC chromatographs of the samples showed that the level of soluble A $\beta$  decreased with increasing lipid concentration (Fig. 14, solid lines), where at a 1:20 A $\beta$  to lipid ratio, no soluble A $\beta$  was present as all A $\beta$  became associated with lipid vesicles. After 11 days of incubation, the amount of soluble A $\beta$  remaining decreased in all samples, including A $\beta$  incubated alone (Fig. 14, dashed lines). ThT



**Figure 15**

Size distribution of POPC vesicles containing 30 mol% POPG, measured by dynamic light scattering, before (●) and immediately after the addition of A $\beta$ . All samples were prepared in water and A $\beta$  concentration was 100  $\mu$ M. Lipid concentration increased from 200 ( $\Delta$ ) to 1000 ( $\square$ ) and 2000 ( $\circ$ )  $\mu$ M, yielding protein to lipid ratios of 1:2, 1:10, and 1:20.

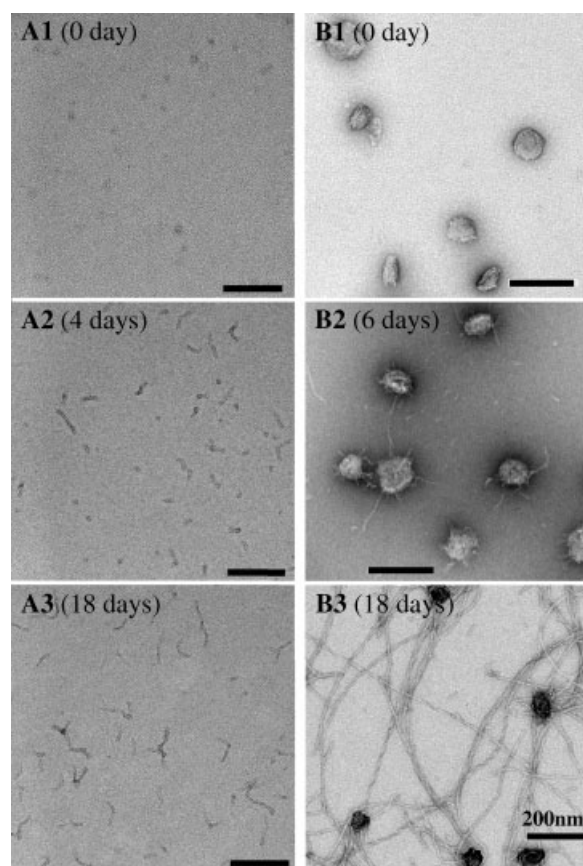
**Figure 16**

Background subtracted ThT fluorescence emission intensity of 100  $\mu$ M A $\beta$  incubated with POPC vesicles containing 30 mol% POPG in water at protein to lipid mole ratios of 1:0 (●), 1:2 (▼), or 1:10 (○).

fluorescence signal of A $\beta$  incubated with lower lipid concentrations are shown in Figure 16. As shown, ThT fluorescence of A $\beta$  incubated alone (filled circles) remained low during 26 days of incubation. Fluorescence signal of A $\beta$  incubated with 1000  $\mu$ M lipids, or 1:10 A $\beta$  to lipid ratio (Fig. 16, open circles), showed an immediate increase in ThT fluorescence that matched the increase observed for 1:20 A $\beta$  to lipid ratio sample [Fig. 13(B), open triangles] followed by no significant increases in ThT fluorescence during 26 days of incubation. As shown in Figure 14, after 11 days of incubation, no soluble A $\beta$  remained for the 1:10 A $\beta$  to lipid ratio sample. Thus, similar to the 1:20 A $\beta$  to lipid ratio sample, adsorption of A $\beta$  to vesicles and the subsequent agglomeration of vesicles were the primary events that took place in the 1:10 A $\beta$  to lipid ratio sample; A $\beta$  fibril formation did not occur to a significant extent with incubation. A $\beta$  incubated with the lowest lipid concentration tested, 200  $\mu$ M, or 1:2 A $\beta$  to lipid ratio, showed a low level of initial adsorption to vesicles (see Fig. 14) and steady increases in ThT fluorescence with incubation time (Fig. 16, filled inverted triangles). After 26 days of incubation, ThT fluorescence signal was at the same level as those observed during A $\beta$  incubation in PBS [Fig. 13(A)], indicating a near complete conversion of A $\beta$  into fibrils.

TEM images of A $\beta$  incubated alone and A $\beta$  incubated at a 1:2 protein to lipid ratio are shown in Figure 17. Samples were diluted five times, adsorbed on glow-discharged carbon-coated support films, stained with 1% uranyl acetate, and dried before imaging. A $\beta$  alone at the start of incubation did not show significant morphology, except for a few small circular features on the TEM micrograph [Fig. 17(A1)]. These could be small oligom-

ers or artifacts from the drying process during sample preparation. After 4 days of incubation, small protofibril-like structures were observed [Fig. 17(A2)] and after 18 days of incubation, these structures were longer and more uniform in length [Fig. 17(A3)]. These protofibril-like structures likely accounted for the loss of soluble A $\beta$  observed during incubation from SE-HPLC results (see Fig. 14). However, these aggregates did not yield ThT fluorescence characteristic of mature fibrils and did not induce the formation of mature fibrils. A $\beta$  incubated with lipid vesicles with a 1:2 protein to lipid ratio at the beginning of incubation showed individual vesicles that were  $\sim$ 100 nm in diameter. Note that vesicles alone, in the absence of any added A $\beta$ , either did not adsorb to the TEM grid or became completely disrupted during drying (data not shown). Thus the vesicles shown in Figure 17(B1) were those associated with A $\beta$ . After 6 days of incubation, fiber-like structures that extended from the vesicles were observed, concomitant with a small increase in ThT fluorescence (see Fig. 16). After 18 days of incubation, a network of fibrils encompassing vesicles

**Figure 17**

TEM images of 100  $\mu$ M A $\beta$  incubated alone (A) or with POPC vesicles containing 30 mol% POPG at a protein to lipid ratio of 1:2 (B).



was observed [Fig. 17(B3)]. The fibrils exhibited twists that are characteristic of mature amyloid fibrils and yielded strong ThT fluorescence signal (see Fig. 16).

## DISCUSSION

The principle finding of this study is that the negatively charged lipid DPPG uniquely templates the folding and assembly of native A $\beta$  that is monomeric and unfolded into  $\sim$ 500 nm  $\beta$ -sheet-like crystalline structures, likely protofibrils, at the lipid membrane-water interface. This finding elucidates the structural dynamics, on the molecular-level, of the early events that may trigger the aggregation of A $\beta$  *in vivo*. Furthermore, we show that these templated A $\beta$  protofibrils at the lipid membrane interface, formed from a sub- $\mu$ M concentration and on 1-h time scale, are capable of inducing the aggregation of A $\beta$  into mature fibrils. This study also provides the direct evidence that the association of A $\beta$  with lipid membrane disrupts lipid packing, implicating that membrane disruption by A $\beta$  as a possible toxicity pathway. Details of these findings are discussed below.

### Mode of A $\beta$ association depends on lipid composition and subphase condition

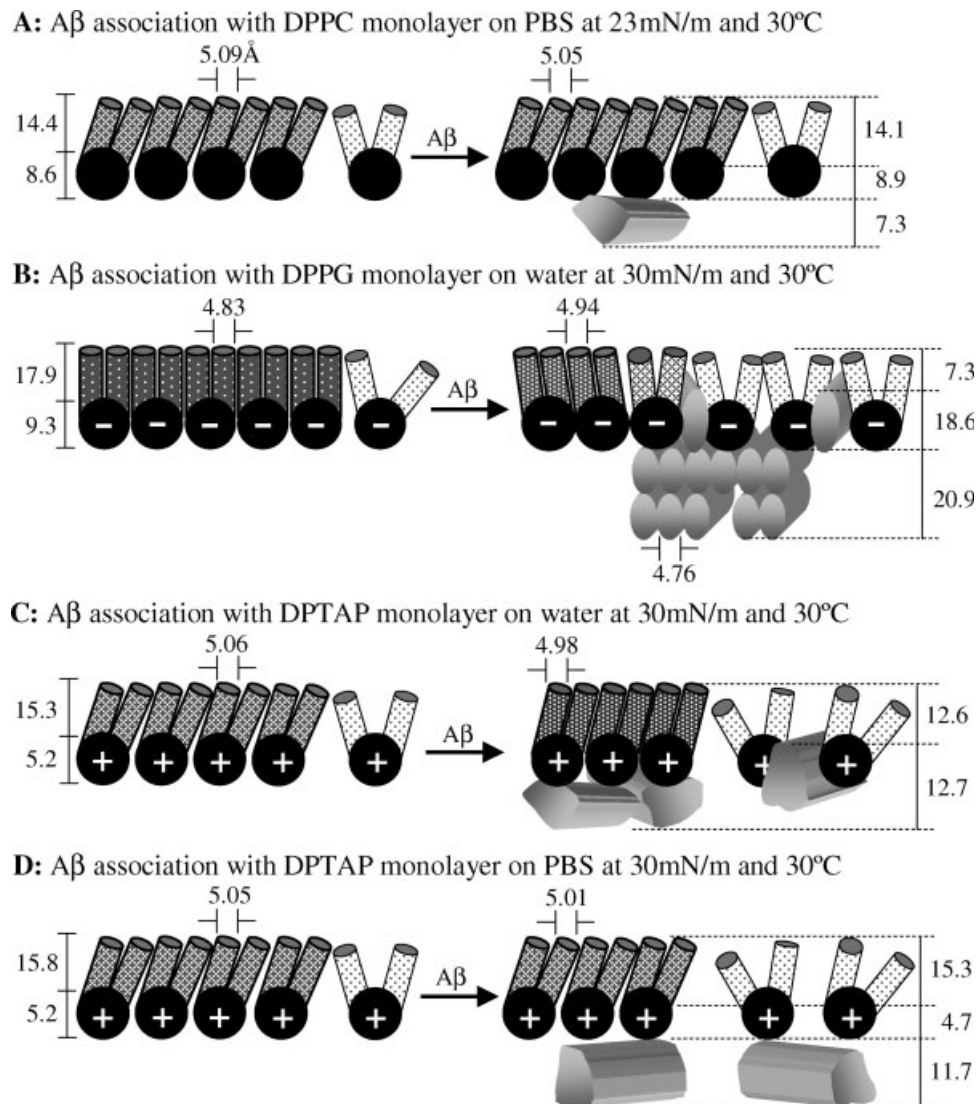
The molecular scale structural details of A $\beta$  associated with DPPC, DPPG, or DPTAP monolayers at 30°C on water and PBS subphases were resolved in this study using a combination of complementary X-ray and neutron scattering techniques. The degree of A $\beta$  penetration into the lipid membrane, the extent of A $\beta$  association with lipid headgroup vs. tail groups, the effect of A $\beta$  association on lipid packing, and the ordering of A $\beta$  at the lipid interface are illustrated in Figure 18. Two cases were not depicted, A $\beta$  associated with DPPC monolayer on water and A $\beta$  associated with DPPG monolayer on PBS, because neither A $\beta$  association nor insertion was detected and no changes in lipid packing were observed. When associated with a lipid monolayer, A $\beta$  exhibited three different modes of interaction: (1) adsorption underneath the lipid headgroups, (2) insertion into the lipid headgroup region, and (3) penetration into the lipid tail region. Since the lipids tested in this study have identical tail groups, the mode of A $\beta$  interaction thus depends on the lipid headgroup and subphase condition, both of which can modulate the electrostatic interactions between A $\beta$  and the lipid headgroup.

The estimated net charge on A $\beta$ 40 based on its amino acid sequence at pH 5.5 (water) and 7.4 (PBS) are 0.2 and  $-2.8$ , respectively (Protein Calculator v3.3, The Scripps Research Institute). Thus, the electrostatic contribution to A $\beta$ -lipid interactions ranges from strongly attractive [charge-charge attraction (e.g., A $\beta$ -DPTAP on PBS)] to moderately attractive [dipole-charge (e.g., A $\beta$ -DPPG on water) and dipole-dipole (e.g., A $\beta$ -DPPC on

water)] to strongly repulsive [charge-charge repulsion (A $\beta$ -DPPG on PBS)].<sup>32</sup> The effect of these interactions is largely reflected in the extent of A $\beta$  insertion into lipid monolayers compressed to a bilayer-equivalent surface pressure, where attractive interactions led to peptide insertion and repulsive interactions prevented A $\beta$  from inserting into the lipid monolayer (Table III).<sup>32</sup> One case, however, does not follow the trend. The insertion of A $\beta$  into a DPTAP monolayer on PBS, where A $\beta$  and DPTAP exhibit strong charge-charge attraction, results in a  $\Delta A/A$  of only 4%, compared with a  $\Delta A/A$  of 35% for A $\beta$  insertion into a DPTAP monolayer on water where A $\beta$  and DPTAP exhibit a weaker charge-dipole interaction.<sup>32</sup> We have hypothesized that the low level of peptide insertion was due to the trapping of the A $\beta$  at the lipid headgroup region from the strong electrostatic interactions. X-ray results from this study provide a direct proof for the hypothesis—the peptide is indeed adsorbed underneath the lipid headgroup [Fig. 18(D)]. As a result, possible stabilization resulting from peptide insertion into the tail region of the lipid, which would give rise to an area increase, did not contribute to the overall A $\beta$ -lipid interaction. In contrast, the weaker dipole-charge interactions between A $\beta$  and lipid headgroup, led to not only adsorption of A $\beta$  to the headgroups, but also insertion into the headgroup region and penetration into the tail groups [Fig. 18(B,C)] that likely stabilizes the hydrophobic C-terminus of the peptide. Moderate interaction with the lipid headgroup thus attracts A $\beta$  to the membrane surface and at the same time, allows additional modes of interaction, such as insertion into the lipid headgroup region and association with lipid tail groups, to occur.

### A $\beta$ disrupts lipid packing

Aside from understanding the different modes of A $\beta$  association with lipid monolayers, the effect of A $\beta$  on lipid ordering is also elucidated. GIXD data show that A $\beta$  disrupts lipid ordering. For all systems studied, with the exception of DPPC on PBS at 30 mN/m where A $\beta$  shows minimal interactions, the presence of A $\beta$  decreases the integrated intensities and increases the FWHM values of the Bragg peaks compared with those of pure lipid films. Such changes result from reductions in the size and number of coherently scattering lipid domains, indicating overall decreases in lipid ordering. For the DPPG monolayer, the coherence length of the 2D lipid crystallites is reduced from 600 Å for the hexagonal phase of the pure lipid to 110 and 250 Å in the two crystallographic directions [(1,0), (0,1)] and  $(-1,1)$ , respectively, with the addition of A $\beta$ . For the DPTAP monolayer, addition of A $\beta$  results in a decrease of coherent length from 400 to 280 Å in the  $(-1,1)$  direction, while coherence length in the [(1,0), (0,1)] direction remained unchanged at 90 Å. The reduction in Bragg peak intensities is also in agree-

**Figure 18**

Schematic of the different modes of A $\beta$  association lipid monolayers. All experiments were carried out at 30°C. The length scales shown in the figure are in Å. The shade of the lipid tail groups depicts ordering, where darker shade corresponds to more ordering and lighter shade corresponds to less ordering. The tilt of the lipid molecules with respect to the normal and lipid tail group spacing are also illustrated.

ment with FM observations where A $\beta$  insertion reduces the area of the condensed phases of the same lipid films from our earlier study.<sup>32</sup>

Disruption of the lipid condensed phase by A $\beta$  insertion is a general phenomenon for all lipids studied, but the peptide exhibits different effects on the unit cell geometry of the lipids. For the DPPG monolayer on water, A $\beta$  causes the unit cell to expand and the lipid tails to tilt when it inserts into the monolayer. However, A $\beta$  insertion into DPTAP monolayer on water and DPPC monolayer on PBS (at 23 mN/m) causes the lipid unit cell to contract. Such opposing effects can be partially explained by the location of the inserted A $\beta$  in these lipid films. From

dual probe fluorescence experiments, A $\beta$  is found to associate with the fluid phase in a DPPG monolayer, whereas for DPTAP, although A $\beta$  interacts with both condensed and fluid phases, its association is predominantly with the condensed phase.<sup>32</sup> For the DPPG monolayer, insertion of A $\beta$  caused the condensed domains in the DPPG monolayer on water to disappear over time and concomitantly, a new gray-color phase, intermediate between dark condensed and bright fluid phases, emerged.<sup>32</sup> X-ray results from this study are in agreement with these findings, where A $\beta$  association with DPPG monolayer led to decreases in DPPG ordering that correlated with increases in A $\beta$  ordering (see Fig. 8). These effects are illustrated in

Figure 18(B). The condensed phase lipids are shown with dark gray lipid-tail groups, the intermediate phase is shown with a medium gray shade and the fluid phase is drawn with a light gray tail groups. For the DPTAP monolayer, the peptide associated with the condensed phase and acted like a multivalent ion that contracts the lipid molecules [Fig. 18(C)].<sup>67</sup>

### DPPG induced folding and templated assembly of A $\beta$ into protofibrils

Our X-ray and neutron scattering data clearly show that folding and assembly can occur for A $\beta$  at a low concentration of 250 nM on a time scale of 1 h. It is clear that A $\beta$  adsorbs to an air–water interface and orders into 2D crystallites. The packing of the peptide is identical to the inter- $\beta$ -sheet distance found in amyloid fibrils by NMR<sup>68</sup> and X-ray fiber diffraction<sup>58</sup> techniques. *In vitro*, amyloid fibrils need days to form at monomer concentrations orders of magnitude higher than the concentration used in this study. The  $\beta$ -sheet ordering observed at the low peptide concentration and the short time scale observed thus is not expected. In addition, the ordering of A $\beta$  can be enhanced by the negatively charged lipid DPPG. The intensity of the ordered A $\beta$  peak is higher when the peptide is associated with a DPPG monolayer than the intensity of the peak obtained from the peptide adsorbed to a bare air–water interface. Moreover, the FWHM of the Bragg peak of A $\beta$  associated with DPPG is narrower, indicating that the ordered A $\beta$  structures are larger, more than double in this case, compared with A $\beta$  structures formed at the bare air–water interface. The enhanced peptide ordering by a negatively charged lipid may serve as the molecular basis for the early events during A $\beta$  fibril formation *in vivo*. Physiologically, anionic lipid-induced fibrillogenesis can occur if these lipids, which normally reside only on the inner leaflet of the cell membrane, become exposed to the outer leaflet due to membrane damage (e.g., oxidative stress).<sup>69</sup>

Additionally, the total thickness of the associated A $\beta$  layer also varied with different lipids. The thickness of A $\beta$  associated with a DPPG monolayer on water is  $\sim 40$  Å. In contrast, A $\beta$  associated with monolayers composed of the lipids DPPC and DPTAP had thickness ranged from 7.3 to 12.7 Å (Table III). Compared with other lipids, DPPG induced not only lateral folding and ordering of A $\beta$ , but also the formation of multi-layers.

To further understand the templating effect of DPPG on A $\beta$  ordering, we tested A $\beta$  association with binary DPPC/PA monolayers. The goal was to create a DPPG-like monolayer by adding negatively charged PA lipid molecules to the neutral DPPC monolayer. In addition to introducing negative charges to the DPPC monolayer, PA, which has a small headgroup compared with its tail group, can act as a “wedge” molecule to the DPPC, which has a larger headgroup compared with its tail, and

help the DPPC molecules to pack more optimally with a smaller tilt of the tail.<sup>50</sup> DPPG has similarly sized (in cross-section) head and tail groups, giving rise to a cylindrical molecule that packs well. Two DPPC/PA compositions were tested: 1:1 and 1:2. The first system still has a larger cross-sectional area for the head region and a lower charge distribution than DPPG: one negative charge for every three acyl chains. The second system mimics the DPPG monolayer well, both in tail group packing (Figs. 7 and 11) and charge density (two negative net charges per four acyl chains). However, neither system induced A $\beta$  ordering, indicating that the templating effect of the DPPG monolayer may be related to specific interactions between DPPG and A $\beta$  or that the negative charge on PA is not sufficiently exposed due to the screening effect of the bulky DPPC headgroups.

### Vesicles containing POPG induced A $\beta$ fibrillogenesis

The characterization of A $\beta$ -lipid interactions and the elucidation of molecular scale structural details give us insights into the nature, strength, and mode of soluble A $\beta$  interaction with lipid monolayers. The aggregation of A $\beta$ , however, seems to be a necessary step for the pathogenesis of AD. One on-pathway product of A $\beta$  aggregation is insoluble fibrils.<sup>1–3</sup> To test the effect of A $\beta$ -lipid interactions on A $\beta$  fibril formation, A $\beta$  was incubated with lipid vesicles composed of POPC, POPC containing 30 mol% POPG, or POPC containing 30 mol% DMTAP. At 100  $\mu$ M, A $\beta$  exhibited a 4-day lag phase followed by rapid fibril growth in PBS. In contrast, A $\beta$  did not undergo fibrillogenesis for up to 26 days in water. A $\beta$  exhibits minimal interaction with DPPC lipids in monolayer studies in either water or PBS, where no insertion was observed at 30 mN/m.<sup>32</sup> The addition of POPC vesicles has no effect on A $\beta$  fibrillogenesis in water and shifts the rapid fibril growth phase 1 day earlier in PBS [Fig. 13(A)]. A $\beta$  exhibits strong electrostatic attraction with DPTAP in PBS and when incubated with POPC/DMTAP vesicles in PBS, the adsorption of A $\beta$  to vesicle surface leads to fibril growth that occurred 2 days earlier than A $\beta$  incubated alone [Fig. 13(A)]. In water, where A $\beta$  associates and inserts into a DPTAP monolayer, incubating A $\beta$  with POPC/DMTAP vesicles does not result in fibril formation. A $\beta$  interacts weakly with DPPG in PBS and incubating with POPC/POPG vesicles does not significantly influence A $\beta$  fibril formation. However, the unique templated  $\beta$ -sheet structures observed on a short time scale (e.g., 1 h) for a low concentration of A $\beta$  at the DPPG monolayer surface on water is found to induce A $\beta$  fibril formation. POPC vesicles containing POPG lipids entirely abolished the lag phase (26 days and longer) and seeded A $\beta$  fibril formation in water. Thus, for all the lipids and solution conditions tested, the only case where the lipid vesicles clearly induced A $\beta$  fibril formation

## ACKNOWLEDGMENTS

## REFERENCES

- PROTEINS
- 23**



35. Chauhan A, Ray I, Chauhan VP. Interaction of amyloid beta-protein with anionic phospholipids: possible involvement of Lys28 and C-terminus aliphatic amino acids. *Neurochem Res* 2000;25:423–429.
36. Zhao H, Tuominen EK, Kinnunen PK. Formation of amyloid fibers triggered by phosphatidylserine-containing membranes. *Biochemistry* 2004;43:10302–10307.
37. Terzi E, Holzemann G, Seelig J. Self-association of beta-amyloid peptide (1–40) in solution and binding to lipid membranes. *J Mol Biol* 1995;252:633–642.
38. Arispe N, Pollard HB, Rojas E. Giant multilevel cation channels formed by Alzheimer-disease amyloid beta-protein [a-beta-P-(1–40)] in bilayer-membranes. *Proc Natl Acad Sci USA* 1993;90:10573–10577.
39. Arispe N, Rojas E, Pollard HB. Alzheimer-disease amyloid beta-protein forms calcium channels in bilayer-membranes—blockade by tromethamine and aluminum. *Proc Natl Acad Sci USA* 1993;90:567–571.
40. Sun XD, Mo ZL, Taylor BM, Epps DE. A slowly formed transient conformer of A beta(1–40) is toxic to inward channels of dissociated hippocampal and cortical neurons of rats. *Neurobiol Dis* 2003;14:567–578.
41. Deshpande A, Mina E, Glabe C, Busciglio J. Different conformations of amyloid beta induce neurotoxicity by distinct mechanisms in human cortical neurons. *J Neurosci* 2006;26:6011–6018.
42. Kaye R, Sokolov Y, Edmonds B, McIntire TM, Milton SC, Hall JE, Glabe CG. Permeabilization of lipid bilayers is a common conformation-dependent activity of soluble amyloid oligomers in protein misfolding diseases. *J Biol Chem* 2004;279:46363–46366.
43. Demuro A, Mina E, Kaye R, Milton SC, Parker I, Glabe CG. Calcium dysregulation and membrane disruption as a ubiquitous neurotoxic mechanism of soluble amyloid oligomers. *J Biol Chem* 2005;280:17294–17300.
44. Seelig A. Local anesthetics and pressure: a comparison of dibucaine binding to lipid monolayers and bilayers. *Biochim Biophys Acta* 1987;899:196–204.
45. Alberts B, Johnson A, Lewis J, Raff M, Roberts K, Walter P. *Molecular biology of the cell*. New York: Garland Science/Taylor & Francis; 2002. p 1463.
46. Als-Nielsen J, Jacquemain D, Kjaer K, Leveiller F, Lahav M, Leisero-witz L. Principles and applications of grazing incidence X-ray and neutron scattering from ordered molecular monolayers at the air-water interface. *Phys Rep* 1994;246:251–313.
47. Jensen TR, Kjaer K. Structural properties and interactions of thin films at the air-liquid interface explored by synchrotron x-ray scattering. In: Mobius D, Miller R, editors. *Novel methods to study interfacial layers*, Vol. 11. *Studies in interface Science*. Amsterdam: Elsevier Science; 2001. p 205–254.
48. Krueger S. Neutron reflection from interfaces with biological and biomimetic materials. *Curr Opin Colloid Interface Sci* 2001;6:111–117.
49. Chi EY, Frey SL, Lee KYC. Ganglioside GM1-mediated amyloid-beta fibrillogenesis and membrane disruption. *Biochemistry* 2007;46:1913–1924.
50. Lee KY, Majewski J, Kuhl TL, Howes PB, Kjaer K, Lipp MM, Waring AJ, Zasadzinski JA, Smith GS. Synchrotron X-ray study of lung surfactant-specific protein SP-B in lipid monolayers. *Biophys J* 2001;81:572–585.
51. Majewski J, Kuhl TL, Kjaer K, Smith GS. Packing of ganglioside-phospholipid monolayers: an X-ray diffraction and reflectivity study. *Biophys J* 2001;81:2707–2715.
52. Wu G, Majewski J, Ege C, Kjaer K, Weygand MJ, Lee KY. Interaction between lipid monolayers and poloxamer 188: an X-ray reflectivity and diffraction study. *Biophys J* 2005;89:3159–3173.
53. Eisenberger P, Marra WC. X-ray-diffraction study of the Ge(001) reconstructed surface. *Phys Rev Lett* 1981;46:1081–1084.
54. Als-Nielsen J, McMorrow D. *Elements of modern X-ray physics*, Vol. 11. New York: Wiley; 2001. p 318.
55. Braslau A, Pershan PS, Swislow G, Ocko BM, Als-Nielsen J. Capillary waves on the surface of simple liquids measured by x-ray reflectivity. *Phys Rev A* 1988;38:2457–2470.
56. Als-Nielsen J, Kjaer K. X-ray reflectivity and diffraction studies of liquid surfaces and surfactant monolayers. In: Riste T, Sherrington D, editors. *Phase transitions in soft condensed matter*. Volume series B: Physics, Vol. 211. New York and London: Plenum Publishing Corporation in cooperation with NATO Scientific Affairs Division; 1989. p 113–143.
57. Petkova AT, Ishii Y, Balbach JJ, Antzutkin ON, Leapman RD, Delaglio F, Tycko R. A structural model for Alzheimer's beta -amyloid fibrils based on experimental constraints from solid state NMR. *Proc Natl Acad Sci USA* 2002;99:16742–16747.
58. Malinchuk SB, Inouye H, Szumowski KE, Kirschner DA. Structural analysis of Alzheimer's beta(1–40) amyloid: protofilament assembly of tubular fibrils. *Biophys J* 1998;74:537–545.
59. Maltseva E, Brezesinski G. Adsorption of amyloid beta (1–40) peptide to phosphatidylethanolamine monolayers. *Chemphyschem* 2004;5:1185–1190.
60. Maltseva E, Kerth A, Blume A, Mohwald H, Brezesinski G. Adsorption of amyloid beta (1–40) peptide at phospholipid monolayers. *Chembiochem* 2005;6:1817–1824.
61. Marquardt DW. An algorithm for the least-squares estimation of nonlinear parameters. *SIAM J Appl Math* 1963;11:431–441.
62. Brezesinski G, Dietrich A, Struth B, Bohm C, Bouwman WG, Kjaer K, Mohwald H. Influence of ether linkages on the structure of double-chain phospholipid monolayers. *Chem Phys Lipids* 1995;76:145–157.
63. Naumann C, Brumm T, Rennie AR, Penfold J, Bayerl TM. Hydration of Dppc monolayers at the air/water interface and its modulation by the nonionic surfactant C(12)E(4)—a neutron reflection study. *Langmuir* 1995;11:3948–3952.
64. Vaknin D, Kjaer K, Alsnielsen J, Losche M. Structural-properties of phosphatidylcholine in a monolayer at the air-water-interface—neutron reflection study and reexamination of x-ray reflection measurements. *Biophys J* 1991;59:1325–1332.
65. McKiernan AE, Ratto TV, Longo ML. Domain growth, shapes, and topology in cationic lipid bilayers on mica by fluorescence and atomic force microscopy. *Biophys J* 2000;79:2605–2615.
66. Kurganov B, Doh M, Arispe N. Aggregation of liposomes induced by the toxic peptides Alzheimer's A beta s, human amylin and prion (106–126): facilitation by membrane-bound G(M1) ganglioside. *Peptides* 2004;25:217–232.
67. Chen V, Evans D, Ninham B. Counterion and co-ion specificity in ionic microemulsions. *J Phys Chem* 1987;91:1823–1826.
68. Benzinger TL, Gregory DM, Burkoth TS, Miller-Auer H, Lynn DG, Botto RE, Meredith SC. Propagating structure of Alzheimer's beta-amyloid(10–35) is parallel beta-sheet with residues in exact register. *Proc Natl Acad Sci USA* 1998;95:13407–13412.
69. Holthuis JC, van Meer G, Huijtema K. Lipid microdomains, lipid translocation and the organization of intracellular membrane transport (Review). *Mol Membr Biol* 2003;20:231–241.